NATURAL RESOURCES

GEOLOGIC MAP OF THE EAGLE GORGE 7.5-MINUTE QUADRANGLE, KING COUNTY, WASHINGTON

by Trevor A. Contreras, Megan L. Anderson, Alec C. Lockett, and Anita L. Bauer

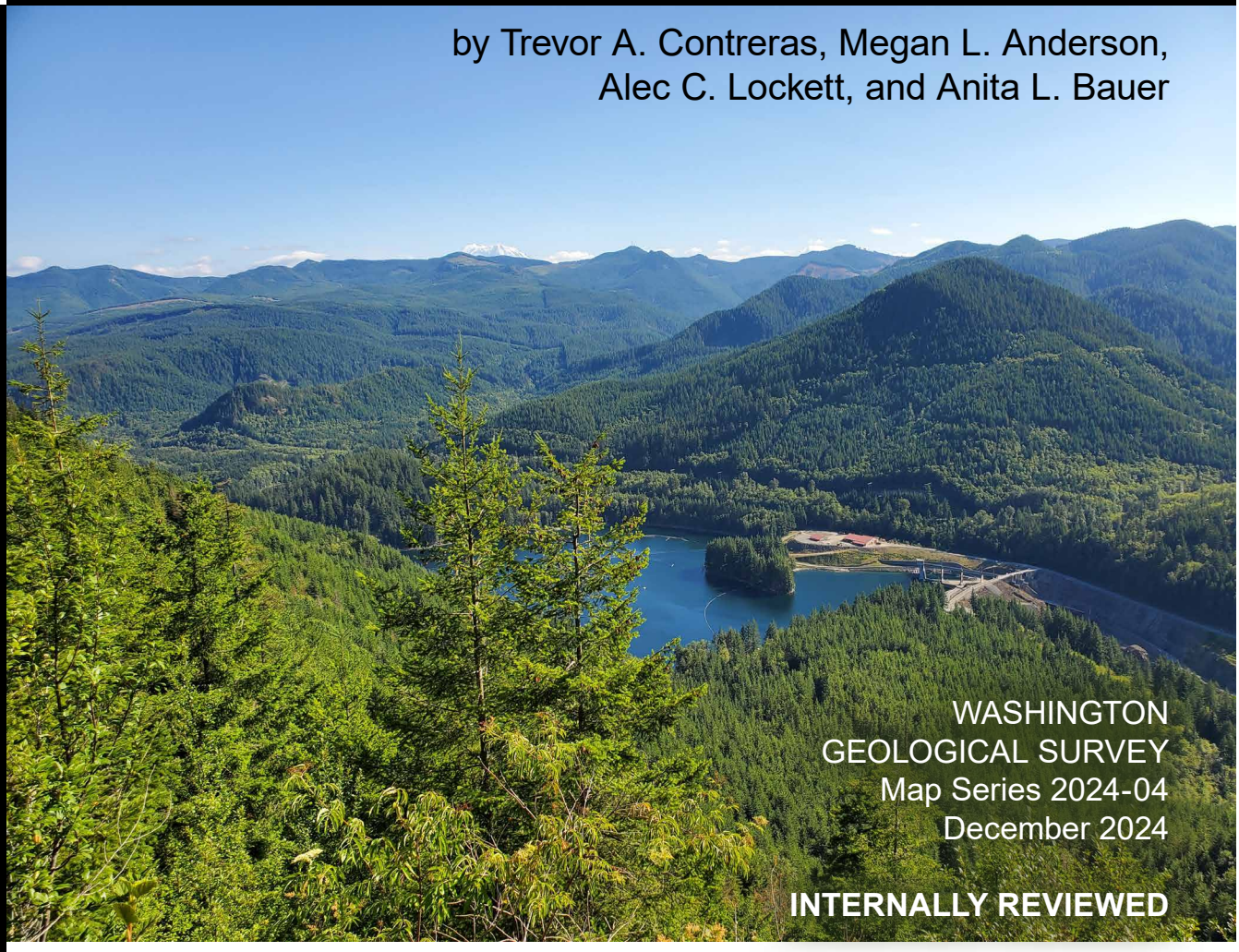

WASHINGTON
GEOLOGICAL SURVEY
Map Series 2024-04
December 2024

INTERNALLY REVIEWED

WASHINGTON STATE DEPARTMENT OF
NATURAL RESOURCES
WASHINGTON GEOLOGICAL SURVEY

GEOLOGIC MAP OF THE EAGLE GORGE 7.5-MINUTE QUADRANGLE, KING COUNTY, WASHINGTON

by Trevor A. Contreras, Megan L. Anderson, Alec C. Lockett, and Anita L. Bauer

WASHINGTON
GEOLOGICAL SURVEY
Map Series 2024-04
December 2024

This geologic map was funded in part by the USGS National Cooperative Geologic Mapping Program, award no. G23AC00468

This publication has been subject to an iterative technical review process by at least one Survey geologist who is not an author. This publication has also been subject to an iterative review process with Survey editors and cartographers.

WASHINGTON STATE DEPARTMENT OF
NATURAL RESOURCES
WASHINGTON GEOLOGICAL SURVEY

DISCLAIMER

Disclaimer of Warranties. No express or implied warranty of any kind is made regarding the information contained herein, including, but not limited to, the warranty of merchantability, warranty of fitness for a particular purpose, or warranties of content, completeness, accuracy, reliability, usefulness, or that use would not infringe on privately-owned rights.

Use at Your Own Risk. The information presented here is intended for use as a general screening tool in community planning or for creating awareness and understanding of geologic information and is neither intended to constitute advice nor is it to be used as a substitute for site-specific advice from a licensed professional. You use this information at your own risk and should not act (or refrain from acting) based upon the information without independently verifying the information and, as appropriate, obtaining professional advice regarding your particular facts and circumstances.

Limitation on Liability. User agrees there shall not be liability on the State of Washington, Washington Department of Natural Resources, or their officers, agents, representatives, or employees for any damages allegedly resulting from any use of or reliance on this information. Under this limitation, there shall be no liability for any damages whatsoever, including but not limited to any damages in contract or tort for compensatory, consequential, punitive, direct, indirect, or special damages such as personal injuries, property damage, loss of profits, or any other losses or expenses.

No Endorsement. Reference herein to any specific commercial product, process, or service by trade name, trademark, manufacturer, or otherwise, does not constitute or imply its endorsement, recommendation, or favoring. Further, the views and opinions of authors expressed herein do not necessarily state or reflect those of the State of Washington or any agency thereof.

INDEMNIFICATION

Research supported by the U.S. Geological Survey, National Cooperative Geologic Mapping Program, under USGS award number G23AC00468. The views and conclusions contained in this document are those of the authors and should not be interpreted as necessarily representing the official policies, either expressed or implied, of the U.S. Government.

WASHINGTON STATE DEPARTMENT OF NATURAL RESOURCES

Hilary S. Franz—*Commissioner of Public Lands*

WASHINGTON GEOLOGICAL SURVEY

Casey R. Hanell—*State Geologist*
Jessica L. Czajkowski—*Assistant State Geologist*
Ana Shafer—*Assistant State Geologist*
Alexander N. Steely—*Assistant State Geologist*

Washington State Department of Natural Resources
Washington Geological Survey

Mailing Address:
1111 Washington St. SE
MS 47007
Olympia, WA 98504-7007

Street Address:
Natural Resources Bldg, Rm 148
1111 Washington St SE
Olympia, WA 98504

Phone: 360-902-1450
Fax: 360-902-1785
Email: geology@dnr.wa.gov
Website: http://www.dnr.wa.gov/geology

Publications and Maps:
www.dnr.wa.gov/programs-and-services/geology/publications-and-data/publications-and-maps

Washington Geology Library Searchable Catalog:
www.dnr.wa.gov/programs-and-services/geology/washington-geology-library

WGS Website

Suggested Citation: Contreras, T. A.; Anderson, M. L.; Lockett, A. C.; Bauer, A. L., 2024, Geologic Map of the Eagle Gorge 7.5-minute Quadrangle, King County, Washington: Washington Geological Survey Map Series 2024-04, 1 sheet, scale 1:24,000, 22 p. text. [https://www.dnr.wa.gov/publications/ger_ms2024-04_geol_map_eagle_gorge_24k.zip]

Cover Photo: Howard A. Hanson Dam. Photo by T. Contreras.

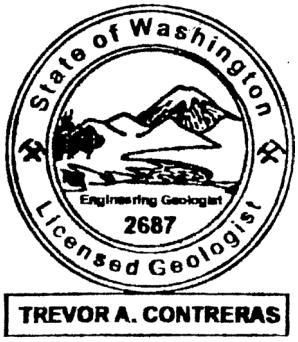

TREVOR A. CONTRERAS

December 2024

Contents

FIGURES

TABLES

MAP SHEET

Geologic Map of the Eagle Gorge 7.5-minute Quadrangle, King County, Washington

by Trevor A. Contreras[1], Megan L. Anderson[1], Alec C. Lockett[1], and Anita L. Bauer[1]

[1] Washington Geological Survey
1111 Washington St SE
MS 47007
Olympia, WA 98504-7007

ABSTRACT

We present a geologic map of the Eagle Gorge quadrangle in Washington's Cascade foothills on the eastern edge of the southern Puget Lowland. We combine new geologic mapping and geophysical modeling to better understand the glacial history, local faulting, and resources in the map area.

Eocene to Miocene sedimentary and volcanic rocks are deformed throughout the map area and mostly dip east in the south and central portions of the map area. Older rocks have steeper dips, suggesting the strata were emplaced while deformation was ongoing.

Geologic mapping and geophysical modeling identify northwest-striking, nearly vertical faults and northwest-striking folds in the northeast corner and along the eastern boundary of the quadrangle. Our geophysical model supports the existence of a northwest-trending, synclinal basin that may have developed during the eruption of Eocene to Miocene volcanic rocks that fill the basin. These rocks are variably deformed, suggesting they experienced progressive deformation that may have continued into the Holocene. However, the evidence for active faulting in the Holocene remains unclear. Northwest-trending scarps in Holocene landslide deposits may be related to faulting or landslide movement in the northeast corner of the map area. Downstream of the Howard A. Hanson Dam, slip occurred on a fault prior to glacial drift being emplaced, as evidenced by alpine drift covering fault gouge that records fault movement.

INTRODUCTION

The map area is in the foothills of the Washington Cascades about 25 mi (40 km) east of Tacoma and 27 mi (44 km) to the north of Mount Rainier (Fig. 1). The landscape of the Eagle Gorge quadrangle is characterized by ridges of Eocene to Miocene volcanic rocks and the valleys of the Green River and Taylor Creek—both drainages are part of the protected watersheds of the cities of Tacoma and Seattle. The area has been sculpted by alpine glaciers at various times during the Pleistocene (Porter, 1976). The Cordilleran ice sheet pushed into the valleys during the most recent continental glacial ice advance ~16 ka (Waitt and Thorson, 1983; Polenz and others, 2015; Haugerud, 2021). The map area is southeast of the Seattle fault and east of the Tacoma fault, while the Rattlesnake Mountain fault zone projects into the northeast corner of the map area; all these faults are considered active (Barnett and others, 2010; Dragovich and others, 2009).

The map area is primarily used for drinking water resources, forestry, and wildlife habitat. The Green River, which passes through the central portion of the map area, is dammed by the Howard A. Hanson Dam and operated by the U.S. Army Corps of Engineers to provide a reservoir for flood control and drinking water for many communities in the southeast Puget Lowland (Tacoma Public Utilities, 2024). Burlington Northern Santa Fe Railway (BNSF) operates trains on the south side of the Green River, an important transportation corridor across the Cascade Range. An active aggregate mine exists on the western boundary of the map, supplying raw materials for development in nearby communities. Coal mining just west of the map area was economically important from the late 1880s to the 1980s (Beikman and others, 1984).

This publication provides insight into geologic hazards (earthquakes and landslides) and natural resources (water and aggregate). It provides information about rock types, geophysical properties, ages, and the processes that formed the landscape—from Eocene deltaic sedimentation and extensive Eocene to Miocene volcanism, to Pleistocene glaciations including both alpine glaciers and continental ice sheets. New geophysical data and modeling provide evidence of subsurface structures and help support our interpretations in the geologic map and cross section.

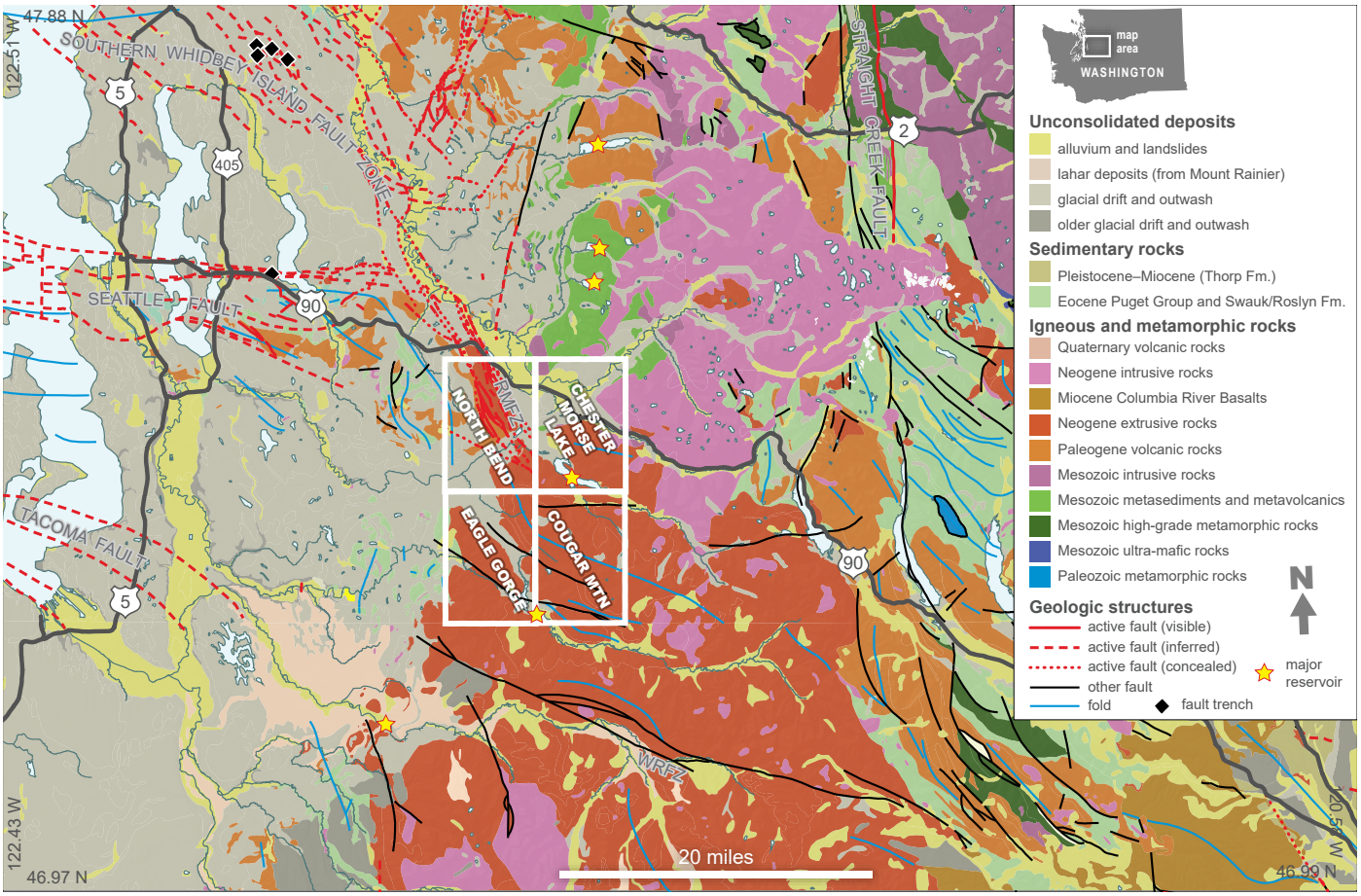

Figure 1. Regional map of the southern Puget Lowland showing surface geology, tectonic structures (RMFZ=Rattlesnake Mountain Fault Zone, WRFZ=White River Fault Zone), and place names in the vicinity of the Eagle Gorge quadrangle.

This map builds on prior mapping in and near the study area that began with work on the nearby coal fields during the 19th century (White, 1888; Willis, 1898) and continued with additional mapping focusing on resources such as coal, clay, silica sand, and mercury (Gower and Wanek, 1963; Vine, 1969; Phillips, 1984) and additional mapping with broader focus at 1:62,500 and 1:100,000 scales (Hammond, 1963; Tabor and others, 2000).

GEOLOGIC OVERVIEW

Bedrock

The oldest rocks in the map area are found in bedrock exposures along the western edge of the quadrangle, and consist of coal-bearing, nonmarine sedimentary rocks of the Puget Group (Vine, 1969). The Puget Group in the area contains Eocene to early Oligocene fossil plants assigned to the upper Kummerian plant stage of Wolfe (1968) and has been dated using K-Ar just west of the map area to >43.4 ±1.9 Ma (Turner and others, 1983). Volcanic rocks above the Puget Group have been most recently mapped as the Ohanapecosh Formation by Tabor and others (2000), but were earlier mapped as the Enumclaw volcanic series by Weaver (1916), as the informal Enumclaw, Huckleberry Mountain, and Snow Creek formations by Hammond (1963), and as unnamed volcanics by Vine (1969). Various authors (Hammond, 1963; Vine, 1969; Tabor and others, 2000) have disagreed about whether an unconformity exists between the Puget Group and the overlying volcanic rocks—Hammond (1963) described an unconformity east of the map area with good exposures of his Mount Catherine tuff, but we did not find the same contact within this map area. The Ohanapecosh Formation consists of multicolored andesitic to dacitic tuff and breccia, volcaniclastic sedimentary rock, and basaltic to andesitic lava flows and mudflows. The Ohanapecosh Formation is more altered than younger rocks up-section and typically exhibits low-grade metamorphism of prehnite-pumpellyite to zeolite facies (Hartman, 1973).

Above the Ohanapecosh Fomation are andesitic to basaltic-andesitic lava flows mapped as volcanic rocks of Eagle Gorge by Tabor and others (2000) and by Hammond (1963) as Eagle Gorge andesite. Above these andesites, in nearby quadrangles, are the Tuff of Stampede Pass and the Tuff of Green Canyon—Oligocene to Miocene tuffs recognized north and east of the Eagle Gorge quadrangle (Hammond, 1963; Tabor and others, 2000; Hammond and Dragovich, 2008; Dragovich and others, 2009). However, we did not find these tuffs in the Eagle Gorge quadrangle.

The volcanic succession is capped by Miocene andesite and basaltic andesite lava flows mapped as Fifes Peak Formation in the adjacent North Bend quadrangle by Dragovich and others (2009)

and by Tabor and others (2000). These were previously mapped by Hammond (1963) as the informal Snow Creek formation.

Unlithified Pleistocene Deposits

Continental glacial deposits cover much of the valleys and lowlands of the map area along the northwest and western edge of the map. The Cordilleran ice sheet left distinct deposits, with sediment derived from the Cascade Range and the Coast Mountains of British Columbia (Armstrong and others, 1965). Most of this lithologically diverse drift was transported into the map area by Cordilleran glacial ice and meltwater during the late Wisconsinan Vashon stade of the Fraser glaciation, when ice reached its southern terminus south of Olympia (Bretz, 1913). Radiocarbon dates suggest that the ice advanced gradually, collapsed quickly, and was only present in the southern Puget Lowland between about 15.3 and 16 ka (Polenz and others, 2015; Haugerud, 2021).

Alpine glaciers that accumulated locally in the Cascade Range left patchy deposits of drift in low relief surfaces in the uplands and in the walls of the Green River valley. This locally sourced drift typically contains more angular clasts than continental glacial drift, which is distinguished by distally sourced clasts not found in the alpine drift and by typically more well-rounded clasts. The alpine drift in the map area is not as well studied, dated, or exposed as the continental drift in the Puget Lowland. Although Crandell and Miller (1974) and Porter (1976) mapped and discussed multiple alpine glacial advances in the central and northern Cascade Range, correlating those regional alpine glaciations with the alpine glacial deposits in the map area has proven difficult due to lack of exposures in the map area that clearly show distinct alpine glacial events.

Regional Structures

A focus of this mapping is to understand how faults and structures in and near the map area are connected, how they have evolved over time, and if any are active. Three known major active fault zones are mapped west and northwest of the quadrangle (Fig. 1): the reverse-slip, east-striking Seattle and Tacoma faults, and the oblique-slip, northwest-striking southern Whidbey Island fault zone (SWIFZ) (Johnson and others, 1999; Brocher and others, 2001; Sherrod and others, 2008; Nelson and others, 2008). The Rattlesnake Mountain fault zone may connect to the aforementioned faults, is interpreted as active (Walsh, 1984; Dragovich and others, 2007 and 2009), and projects into the map area (Fig. 1). Together, these faults accommodate north-south shortening of the Cascadia forearc (Wells and others, 1998). The last known rupture on the Seattle fault occurred 923–924 AD—concurrent with ruptures on other faults on the west side of the Puget Lowland (Black and others, 2023). Closer to the map area, Willis (1889) noted deformation of the Puget Group into north-trending folds and overthrusts west of the Eagle Gorge quadrangle based on coal mine exploration records. Hammond (1963) mapped northwest-trending faults and synclines in the map area.

Tabor and others (2000) constructed cross sections through the region and interpreted the major structural features to be a series of NW-striking mostly reverse faults with related anticlines and synclines, and, following Hammond (1963), show those as being active during the Oligocene through the latest Miocene.

METHODS

Geologic Mapping

We identified units from field observations in the Eagle Gorge and the adjacent Cougar Mountain quadrangles in the summer and fall of 2023. Field work was conducted in both quadrangles, and the work in the Cougar Mountain quadrangle informs our mapping in the Eagle Gorge quadrangle. We collected field data and constructed preliminary field-based maps using tablets equipped with GPS. We refined our field mapping through petrographic review of thin sections; geochemical analyses; U-Pb dating of zircon; radiocarbon dating; geophysical measurements; analysis of well and boring records; and consideration of prior geologic mapping, aerial orthophotos, and identification of geomorphic features from lidar. We used a lidar-based bare-earth digital elevation model (DEM) with a 1.5-ft grid resolution (Washington Geological Survey, 2022) to estimate site elevations and derive hillshade images and other products to map landslides, alluvial fans, and talus. Additionally, we compiled landslides and alluvial fans from Mickelson and others (2019), only modifying their mapping where needed to comply with map scale, or where more detailed lidar data supported mapping additional landslides. The landslides we mapped and those of Mickelson and others (2019) are differentiated within our GIS data by notes indicating the source of the mapping.

During our mapping, we collected ~500 new outcrop observations including 231 new measurements of bedding or flow foliation in volcanic units and fault orientations. We compiled some bedding and flow foliation measurements from Hammond (1963), Phillips (1984), and Tabor and others (2000). Compiled data are identified in the GIS and are shown where located by the original authors or georeferenced by us. In volcanic units we used the 'bedding' symbol where we measured bedding in volcaniclastic deposits, and the 'flow foliation' symbol where we measured an orientation of flow banding or foliation that we were confident represented dip of the volcanic strata. Due to scale, not all orientations are shown on the map, but all are included in the GIS data. We made 22 thin sections and analyzed 12 samples for geochemistry to better identify and describe the geologic units. We reviewed well reports and hydrogeology studies from the City of Tacoma for their North Fork well field to understand the stratigraphy of the glacial deposits in the North Fork Green River valley (Noble, 1969; City of Tacoma, written commun., 2023) and a geothermal borehole log (Washington Geological Survey, 2024) to evaluate thickness of the Puget Group along the western edge of the map boundary.

Potential-Fields Geophysical Methods

We collected 251 new gravity measurements to construct a refined gravity map with ~1 km grid spacing and a profile with approximately 250 m between measurements along the cross-section line. We applied a quantitative curvature analysis algorithm to the gravity data to select high-amplitude, linear gradients, or 'max-spots' for interpretation (Appendix A; Fig M1A). Aeromagnetic

data are from Blakely and others (1999); mapped aeromagnetic anomalies (Fig. M1A) help distinguish different types of volcanic rocks in the subsurface. We used iterative forward modeling of isostatic gravity and aeromagnetic profiles (using GM-SYS, Geosoft, Inc.) along line X–X′ (Fig. M1B) to quantitatively test subsurface interpretations developed from map-view data. Rock density and magnetic susceptibility measurements of samples from 42 new outcrops within and just outside the map area (see Data Supplement) in addition to rock property data collected previously in the region (Steely and others, 2022; Anderson and others, 2024) helped constrain the geophysical models. Appendix A contains details of gravity, magnetic, rock property, and modeling methods.

Geochronology and Geochemistry

We use the geologic time scale of Walker and Geissman (2022) and work by Berggren and others (1985, 1995) to differentiate epochs.

To better understand the ages of units, we used U-Pb dating of zircon. This helped to determine the crystallization ages of an intrusive body (GD1) and to constrain the depositional ages of sedimentary beds using detrital zircon (GD2). See Appendix B for results.

We used radiocarbon dating in an attempt to date glacial sediment in the Green River valley (age site GD3). A carbonized piece of wood was collected, dried, manually cleaned to remove dirt from the sample, and the outer layers removed from the sample to reduce potential for contamination. The sample was then weighed, packaged, and shipped to a commercial radiocarbon dating company using their sample submission recommendations (DirectAMS, 2023).

We analyzed major and trace element geochemistry for 12 samples to assist with rock classification and characterization. This included whole rock inductively coupled plasma atomic emission spectroscopy (ICP-AES), loss on ignition (LOI), and inductively coupled plasma mass spectroscopy (ICP-MS) with methods outlined in Appendix C. Sample sites are depicted on the map and results included in the Data Supplement.

DESCRIPTION OF MAP UNITS

Holocene to Pleistocene Postglacial Deposits

af **Artificial fill (Holocene)**—Mixed earth materials of varied grain size and sorting placed to elevate the land or modify topography; may contain crushed rock, organic material, concrete, or debris; may be engineered; loose to compact; shown where thick and (or) extensive; differentiated from modified land by greater thickness and a composition that differs from that of the underlying geologic unit. Mapped predominantly at the Howard A. Hanson Dam, along the BNSF railway, and at a stockpile area north of the Tacoma Water Supply Intake.

ml **Modified land (Holocene)**—Mixed earth materials of varied grain size and sorting; modified by humans; typically modifies other unconsolidated deposits; may contain organic material, concrete, or debris; may be engineered; loose to compact; shown where thick and (or) extensive; differentiated from artificial fill by a composition that matches the underlying geologic unit (though other original characteristics, such as bedding, may no longer be recognizable). Mapped predominantly at dam and water treatment facilities, landslide repairs, and gravel pits.

Qa **Alluvium (Holocene to Pleistocene)**—Unconsolidated gravel, sand, and silt in varied amounts; mapped in active river and stream channels and floodplains; alluvium is mapped from lidar and differentiated from outwash deposits where more distinct younger channels are observed, the distinction is ambiguous in places; primarily mapped along the Green River, Taylor Creek, Coal Creek, and Charley Creek; Unit Qa is mapped as Holocene because Pleistocene glacial ice and processes would have impacted the valleys where this unit is mapped.

Qb **Beach deposits and alluvium (Holocene)**—Sand, locally interbedded with varying amounts of silt, pebbles, cobbles, and boulders; mapped along the shores of Howard A. Hanson Reservoir in the eastern portion of the quadrangle; includes some alluvium where streams enter the reservoir and their alluvium is modified by changes in water level and wave action.

Qp **Peat (Holocene to Pleistocene)**—Organic and organic-rich sediment including peat, gyttja, muck, silt, clay, and sand; mapped where lidar reveals flat areas and closed depressions, and in areas where we interpret hydrophilic vegetation or wet conditions without trees, based on aerial photos. Two areas are mapped as peat within a landslide deposit on the west side of the map, north of the Green River.

Qaf **Alluvial fan (Holocene to late Pleistocene)**—Varied amounts of pebble to cobble gravel, boulders, and sand with minor silt; generally unconsolidated and moderately to poorly sorted; thickness varies from a few meters on smaller fans to 25 m on well-developed fans in the North Fork Green River valley; mapped throughout the area where stream channels become unconfined and transition into a characteristic fan-shaped landform that can be observed in lidar. Formed by deposition of sediment from flooding, debris flows, shallow landslides, and alluvial processes. Some mapped fans may be inactive in the current climatic regime; however, we were unable to separate inactive fans from active fans due to a lack of obvious incision or activity in lidar and aerial photos. Site-specific evaluation would be needed to determine whether a particular fan is active.

Qls **Landslide deposits (Holocene to Pleistocene)**—Sand, silt, clay, pebbles, cobbles, and boulders, in varied amounts, derived from rocks and deposits upslope; mostly loose, unsorted, and jumbled; mapped from

Table 1. Summary of geochronology. Uncertainties are provided at 2-sigma (95%) confidence.

Sample	Map Unit	Method	Material	Age ±2σ	Age Type	Notes	Source
GD1	ΦEva$_o$	U-Pb	Zircon	<35.8 ±0.4 Ma	Maximum depositional age of sandstone	Colocated analyses G7 & TS13	This report
GD2	Migbd	U-Pb	Zircon	18.9 ±0.2 Ma	Cooling age of intrusion	Colocated analyses G10 & TS18	This report
GD3	Qgo	^{14}C	Carbonized wood	42,018 ±375 cal yr BP	Detrital carbon	Age is too old for deposit	This report
GD4	ΦEva$_o$	K-Ar	Whole rock	33.1 ±1.7 Ma	K-Ar on andesite flow	---	Phillips (1984)

landforms expressed in lidar. Some landslides were mapped by Mickelson and others (2019) and their features are limited to their study area footprints—approximately the western third and northeastern corner of the map area. We modified some of their boundaries to conform with map-scale constraints and nearby map units. We added some landslides within their study area footprint due to having access to more recent, higher-resolution lidar data, which allowed for improved recognition of landslide landforms. We query this unit where landslide forms were evident but questionable. The queried landslides were dominantly mapped where melting continental glacial ice may have caused slumping of previously ice-buttressed glacial deposits north of McDonald Mountain and other locations associated with older alpine glacial deposits around the South Fork of the Cedar River that have landslide characteristics like hummocky topography. Absence of a mapped landslide does not indicate the absence of landslide hazard.

Qct **Colluvium and talus deposits (Holocene to Pleistocene)**—Loose soil, gravel, cobbles and boulders, sand, silt, and clay, all in varied amounts, deposited by shallow ravel and soil creep or rock fall; locally includes colluvium and small landslides; thickness is poorly constrained but is likely ~1–20 m based on rough estimates from lidar (approximating the underlying slope and comparing it with existing topography to get an estimated thickness); deposits are mapped along the base of steep rocky cliffs throughout the quadrangle; identified from lidar and shown where colluvium or talus covers the underlying units; unit Qct is mostly Holocene but some deposits may include older talus that formed during colder climatic periods of the Pleistocene.

Late Pleistocene Glacial Deposits

The Puget lobe of the Cordilleran ice sheet advanced to its southern terminus, located approximately 100 km southwest of the map area (Bretz, 1913; Polenz and others, 2018), during the late Wisconsinan Vashon stade of the Fraser glaciation (Armstong and others, 1965). Previous nearby mapping by Mackin (1941), Booth (1990), Dragovich and others (2009), and Steely and others (2022) suggests that at the northern edge of the map area, the Puget lobe covered the landscape below 2,000 to 2,200 feet elevation. Booth (1990) studied the extent of ice in nearby valleys and how the ice dammed them and formed embankments and glacial lakes. Based on the ages of samples from the the Issaquah delta (Porter and Swanson, 1998), and recalibrated by Haugerud (2021), we estimate that Vashon ice and associated Vashon Drift entered the map area after about 17.6 to 17.7 ka. We map glacial drift from the Puget lobe up to elevations of approximately 2,100 feet on the northwest edge of the map area. The Puget lobe transported a diverse assortment of rock types from British Columbia and the North Cascades, including metamorphic and granitoid clasts sourced from north of the map area. We call this diverse assemblage of clasts 'exotic' or 'distally sourced' because the rock types within them are uncommon or absent in the map area; and these clasts are commonly more rounded compared to locally derived clasts.

Field relationships indicate that an alpine glacial advance in the Cascade Range preceded the continental ice sheet advance. The Puget lobe and the alpine glaciers did not touch during the most recent maximum extent of the Puget lobe as inferred from cross-cutting relationships and dating of the deposits (Mackin, 1941; Crandell, 1963; Porter, 1976). Crandell (1963) mapped relatively fresh alpine drift, termed 'Evans Creek drift' approximately 30 km south-southeast of the map area for deposits related to alpine valley glaciers that extended from the Mount Rainier area early in the Fraser glaciation. The Evans Creek drift preceded the Puget lobe's advance based on mapping in nearby areas (Crandell, 1963; Porter, 1976). Within the map area we found alpine drift that was weathered and located in areas not associated with obvious cirques or moraines. The drift appeared more weathered than we would expect based on Crandell's descriptions of Evans Creek drift, and thus it is likely older. We've mapped this alpine drift as unit Qapd.

VASHON DRIFT

Qgo **Recessional outwash, undivided (late Pleistocene)**—Pebble gravel and sand, less commonly includes cobble and boulder gravel; light tan brown to light gray brown, or variegated with iron and silica cement; loose; well rounded to subangular; poorly sorted to well sorted; gravel is clast supported but locally it has a matrix of sand and silt, and interbeds of laminated silt and sand; gravel and sand have planar bedding; based on lidar and well reports the thickness is estimated to be 25–50 m; mapped in gently sloping outwash channels along Taylor Creek, and along both the North Fork and main stem of the Green River; based on well and hydrogeology

reports from the North Fork well field (Noble, 1969) older alpine glacial deposits (unit Qapd) and glacial lacustrine deposits (unit Qgl) underlie this unit; unit Qgo includes both locally derived and exotic clasts suggesting it is sourced from both continental and alpine glacial sources. Differentiation between continental and alpine glacial deposits relied on observing a diversity of clasts, including granitic clasts that are not found upstream in the Green River drainage. These clasts are also more rounded than those in the alpine drift. Alpine drift is dominated by andesite and volcaniclastic clasts that are less rounded and thus less mature than clasts in the continental drift. Locally used for aggregate. Subdivided into:

Qgos **Recessional outwash sand (late Pleistocene)**—Sand and silt; light brown; loose; subrounded fine sand; well sorted; at least 25 m thick and mapped on distinct terraces between 1,170 and 1,250 ft in elevation upstream of the Howard A. Hanson Dam in the Green River valley; inset against glacial lake deposits (Qgl), indicating that unit Qgos formed during or after draining of the glacial lake represented by Qgl.

Qgl **Glaciolacustrine deposits (late Pleistocene)**—Sand and silt with minor clay and rare diamicton containing pebbles and cobbles; light brown to light gray; compact and stiff; subrounded clasts; well sorted to poorly sorted; planar-laminated beds of silt and structureless sand, locally includes diamicton and beds of silt, including subrounded exotic pebbles that we interpret as dropstones; the unit is estimated from exposures to be 45–60 m thick and may be thicker; mapped in the Green River valley both up and downstream of the Howard Hanson Dam; deposited in glacial lakes when the valleys were blocked by the Cordilleran ice sheet; deposited on top of alpine drift and bedrock, and overlain by glacial outwash (unit Qgo); we infer the age of unit Qgl to be younger than about 17.7 ka and older than 15.5 ka (Porter and Swanson, 1998; Haugerud, 2021).

Qgd **Glacial embankment (late Pleistocene)**—Sandy pebble to cobble gravel, with sparse pebble to boulder diamicton (till) and minor interbedded clayey silt; tan to light gray; sand and gravel are loose to dense and till and silt are very stiff; clasts are subrounded to rounded and exotic clasts are common; sorting varies from unsorted diamicton to well-sorted sand and gravel; estimated to be up to 90 m thick based on lidar by subtracting a lower elevation from a nearby stream channel from the top elevation of the embankment; Booth (1986) studied nearby drainages and suggested that these deposits are the result of subglacial deposition into a glacially impounded lake near the ice limit during glacial maximum. A few queried polygons, mapped remotely using lidar, are on benches just below 1,500 ft that appear to be associated with a glacial lake or moraines in the North Fork Green River valley and their origin is unclear.

Qgic **Ice contact deposits (late Pleistocene)**—Stagnant ice deposits, consisting of ablation till, kame deposits, subglacial outwash, and rare lodgment till; primarily loose to compact silty diamicton, with minor sandy pebble to cobble gravels; color is generally light gray to light brown gray; grain size in the diamicton ranges from silt to boulder; clasts are generally subrounded but may include rare faceted and subangular clasts; typically a chaotic mixture of variably sorted and bedded sediment and diamicton; typically forms a veneer up to 15 m thick on the fluted lowlands in the northwest corner where nearly west–east-oriented drumlins are observed in lidar, and up to 100 m thick along the Green River near Palmer based on lidar elevation estimates and exposures west of the map area; mapped along the western edge of the map where we interpret the deposits as being formed by the Puget lobe when it pushed into the Green River main stem and North Fork; clast lithologies are diverse and include rare distally sourced clasts (metamorphic and granitoid clasts), which suggest they were transported by the Puget lobe from elsewhere. The geomorphic character of unit Qgic includes drumlins and irregular hummocky landforms, such as kames and kettles, that suggest the unit was deposited as the ice sheet stagnated and melted. In the northwest corner of the map, drumlins are east-trending, while drumlins farther west are southeast-trending, suggesting Puget lobe flowlines curved from southerly to southeasterly as ice flowed into the map area. Unit Qgic blankets older bedrock and possibly (unmapped) Vashon advance outwash deposits along the edge of the advancing ice sheet as mapped by Dragovich (2009) in the North Bend quadrangle. We infer the age of unit Qgic to be about 16.0 to 15.5 ka, based on Polenz and others (2015) and Haugerud (2021).

PRE-VASHON ALPINE DRIFT

Qapd **Glacial drift, alpine (Pleistocene)**—Diamicton with boulders to pebbles in a matrix of sand to clay, and stratified drift of clay, silt, sand, and pebble and cobble gravel; tan to brown and red brown; soft to stiff and loose to dense; clasts subangular to subrounded and commonly more subangular; poorly to moderately sorted; commonly, a thin veneer of unsorted oxidized diamicton in the uplands, and up to 100 m of bedded silt, sand, ash altered to clay, and diamicton in the Green River valley; mapped in the Green River valley where deposits include glaciolacustrine drift, outwash, alpine till, and colluvium, and in the higher topography where there are discontinuous patches of diamicton on bedrock; mapped from lidar and sparse field observations of alpine drift in the uplands, that in lidar appear as relatively smooth surfaces between rough bedrock exposures; due to limited exposures of alpine drift and difficulty in differentiating it in lidar, it is likely more extensive than

mapped. We infer that unit Qapd was deposited by or near alpine glaciers on top of pre-existing alluvium, drift, and bedrock as it overlies bedrock in the uplands and diverse deposits in the valley. Varied clast weathering and degrees of soil development suggest that unit Qapd may include deposits from multiple alpine ice advances prior to the Fraser glaciation, similar to findings of Tabor and others (2000). Unit Qapd probably predates the Evans Creek drift of Crandell (1963) because of the presence of ash altered to clay and the more advanced state of weathering than would be expected for Evans Creek Drift based on its appearance in nearby areas. However, we lack direct age control. Unit Qapd is queried where inferred from lidar alone, without nearby field observations, and based on smoothed topography in the uplands of the map area.

Tertiary Bedrock Units

INTRUSIVE ROCKS

Migbd **Gabbroic diorite (Miocene)**—Gray, equigranular gabbroic diorite (geochemistry site G10, SiO_2 = 54.6%); phenocrysts of plagioclase, hornblende, and pyroxene; weathers pale yellow gray; well indurated; plagioclase crystals are anhedral to subhedral, typically 2–3 mm and range to 4 mm; blocky planar joints; in thin section (thin section site TS17), pyroxene-iron symplectites are prevalent and occur around subhedral plagioclase. Mapped only in a small area of a landslide headscarp 1 km northeast of the Howard A. Hanson Dam where it intrudes unit Ovc_o. Zircons from this unit have a crystallization age of 18.9 ±0.2 Ma (age site GD2), suggesting crystallization of the diorite at that time.

MOii **Andesite dikes (Miocene to Oligocene)(line unit only)**—Aphanitic to moderately porphyritic andesite; gray to black and green gray; weathers light tan and brown; well indurated; jointing is locally prominent and blocky, parallel and subperpendicular to the intrusive contact; most phenocrysts are 1–3 mm long; thin sections reveal phenocrysts are subhedral plagioclase with sparse subhedral to anhedral clinopyroxene. The groundmass is dark and cryptocrystalline and alteration minerals include clay (possibly smectite), iron oxides, calcite, and zeolites. Dike widths vary from 15 cm to 3 m and alteration of host rock is often less than 25 cm wide. This unit was only recognized in the central part of the map area along the ridge between the North Fork Green River Valley and the main stem of the Green River where it intrudes unit Ovc_o. This unit is depicted on the map plate as a red dike symbol. We interpret this unit as the feeder dikes for unit Mva_{fp} and perhaps the earlier Oligocene volcanic flows of unit Ova_{eg}. If this is correct, then this unit is likely more widespread than currently mapped.

VOLCANIC AND SEDIMENTARY ROCKS

Mva_{fp} **Fifes Peak Formation (Miocene)**—Andesite to basalt and minor flow breccia; andesite to basaltic andesite is aphanitic and gray, dark gray, or dark red brown; basalt is porphyritic and dark gray to black; flow breccia is brown red; weathers to light gray, gray brown, brown, or red; flows are well indurated and breccia is variable and can be friable; jointing in lava flows is platy or occasionally produces wavy crude columns, vesicular flow tops are rare; in thin section, andesite contains phenocrysts of plagioclase, clinopyroxene, and less abundant hypersthene; the plagioclase and pyroxene exhibit oscillatory zoning in some samples; basaltic andesite and basalt have weakly developed flow banding and are microporphyritic to porphyritic with plagioclase phenocrysts up to 5 mm; flows are altered to heulandite and clay but lack the abundant prehnite observed in flows from older units (Hartman, 1973); individual flows are approximately 10–30 m thick; the unit is estimated to be 460 m thick along cross section A–A′; unit is mapped in the northeast corner of the quadrangle; Hartman (1973) interpreted that the unit erupted from Miocene shield volcanos; the lava was emplaced on top of andesite (unit Ova_{eg}) on an erosional unconformity according to Hammond (1963) and is faulted and deformed into a tight syncline. As mapped, unit Mva_{fp} includes the upper portion of Hammond's Cougar Mountain and Snow Creek formations. This unit is Miocene based on several lines of evidence: (1) they are the least altered package of volcanic rocks in the area; (2) they overlie Oligocene and Eocene rocks along a pronounced angular unconformity; (3) Tabor and others (2000) provide K-Ar ages of 20–24 Ma for their Fifes Peak formation, and Hammond and Dragovich (2008) report an $^{40}Ar/^{39}Ar$ age from the underlying tuff of Green Canyon that provides a lower limiting age of 23.41 Ma.

Ova_{eg} **Andesite flows of Eagle Gorge (Oligocene?)**—Andesite, basaltic andesite, basalt, breccia flows, and minor tuff-breccia; typically gray, dark blue gray to black; weathers to a light brown and grayish red; flows are aphanitic to porphyritic and are 5–10 m thick, exhibit blocky and platy jointing, crude columnar jointing, and rarely have vesicular tops; thickness of unit is estimated at 1,400–2,050 m along cross sections A–A′ and B–B′ respectively; unit is mapped along the eastern third of the map area; according to Hammond (1963) unconformities exist both below and above this unit and this unit erupted onto the volcaniclastics of unit Ovc_o; in thin section, andesite contains glomerocrysts of plagioclase and clinopyroxene with intergranular to intersertal texture and includes minor hornblende; alteration minerals include hematite, clay (smectite), calcite, chlorite, and heulandite; amygdules and veins of chalcedony are common; andesite is fairly fresh in hand sample, but pyroxene is altered; overall the andesite is less altered than underlying flows in units OEva_o; included in this unit are rocks Hammond (1963)

mapped as Eagle Gorge andesite, Snow Creek formation, and Cougar Mountain formation. We assign this unit an Oligocene age based on three dates from overlying tuffs in the Cougar Mountain quadrangle that span approximately 23.6–20.8 Ma (Tabor and others, 2000; Hammond and Dragovich, 2008) and the observation that rocks of this unit overlie Oligocene to Eocene age rocks.

Tvs$_{eg}$ Sedimentary volcanic sandstone and conglomerate of Eagle Gorge (Oligocene?)(line unit only)—Sandstone is gray to tan buff and consists of feldspar and pumice fragments; conglomerate is brown, consisting of andesite clasts; indurated to friable; sandstone contains local minor stringers of pebbles and is well sorted; conglomerate is poorly sorted; sandstone and conglomerate are well bedded; conglomerate consists of cobbles to boulders up to 1 m in diameter with a sandy matrix; includes approximately 120 m of sedimentary rocks as estimated from two exposures near the eastern map boundary but it is likely thicker and more extensive to the east as mapped by Hammond (1963) as part of his volcanic sediments of Cougar Mountain formation; unit Tvs$_{eg}$ is mapped in two locations as a line unit: (1) near the eastern map boundary, southwest of Ghost Point, and (2) in the northeast corner of the map area near the contact with unit Mva$_{fp}$; unit Tvs$_{eg}$ is part of Hammond's (1963) Cougar Mountain formation in which he noted plant and wood fossils, though we did not observe any during our mapping.

Late Eocene to Oligocene Ohanapecosh Formation

In the map area, the Eocene to Oligocene volcanic succession overlying the Puget Group has been called the Enumclaw volcanic series of Weaver (1916), Keechelus andesitic series of Smith and Calkins (1906) and as mapped by Warren and others (1945), unnamed volcanics of Gower and Wanek (1963), the Huckleberry and the Enumclaw formations of Hammond (1963), unnamed volcanics of Vine (1969), and unnamed rocks by Phillips (1984). Tabor and others (2000) grouped these rocks together in the Ohanapecosh Formation of Fiske and others (1963). We continue this use of Ohanapecosh Formation, but due to the differences in map scale, we divide the volcanic sequence into two units, a volcaniclastic-dominated unit Tvc$_o$ and a flow-dominated unit TEva$_o$. Due to changes in the definition of the Eocene–Oligocene boundary from 36.6 to 33.9 Ma based on Berggren and others (1985, 1995) and U-Pb age control at the base of the Ohanapecosh Formation of 35.8 Ma (age site GD1), we assign at least the lower portion of the unit to the Eocene. This Eocene age differs from Tabor and others (2000), who used the time scale of Berggren and others (1985) to assign the unit to the Oligocene. We map the upper volcaniclastic unit as Oligocene but the lower, flow-dominated unit as Eocene to Oligocene based on ages of these rocks within the map area (age sites GD1 and GD4). The Ohanapecosh Formation underwent low-grade metamorphism, accounting for an abundance of prehnite (Hartman, 1973). Because water is required for prehnite-forming alteration, these rocks were either deposited in water or interacted with fluids after burial (Hartman, 1973). Furthermore, volatiles, specifically methane, produced from heating of coal within the underlying Puget Group, may have inhibited zeolite production that would otherwise commonly be associated with prehnite-forming alteration (Hartman, 1973). However, since lavas have low porosity and permeability, prehnite in interbedded lavas would be preserved (Hartman, 1973).

Tvc$_o$ Volcaniclastic rocks (Oligocene)—Lithic tuff-breccia, lapilli tuff, pebbly diamictite, tuffaceous siltstone, and minor andesite flows; multicolored, includes brown, blueish green, green, tan, purple, blue, pink, and white rocks; moderately indurated to friable; the tuff, breccia, and diamictite typically contain angular clasts of pumice, andesite porphyry, dacite, minor basalt, and rare carbonized wood fragments; well bedded with moderately well-defined, large-scale bedding typical in massive diamictons and siltstone beds that are finely bedded to laminated; prominent spheroidal weathering in some volcaniclastic mudflows and tuffs; andesite is dark gray, largely aphanitic, and exists in isolated flows; we estimate the thickness of the unit along cross section B–B′ as approximately 1,800 m. This volcaniclastic unit grades westward into andesite flows with minor volcaniclastics (unit TEva$_o$) in the central part of the quadrangle. Unit Tvc$_o$ was mapped by Tabor and others (2000) as Ohanapecosh Formation and correlates with the Huckleberry Mountain formation of Hammond (1963). Unit Tvc$_o$ is locally intruded by dikes and small intrusions of andesite (unit MOii) and gabbroic diorite (unit Migbd). This unit is considered Oligocene because the underlying unit is latest Eocene to early Oligocene.

TEva$_o$ Andesite flows (late Eocene to Oligocene)—Andesite flows, flow-breccia, minor tuff-breccia, rhyodacite tuff, and basalt; locally includes minor volcaniclastic sandstone and carbonaceous siltstone near the base; andesite is dark green gray, weathering to light brown gray; well indurated; aphanitic to porphyritic; flows are blocky, platy, and have crude to well-developed columnar jointing; poor to moderately developed flow banding; rare vesicles; in thin section andesites are commonly amygdaloidal, consisting of altered phenocrysts in a groundmass of feldspar microlites embedded in glass (hyalopilitic) and include alteration minerals of calcite, prehnite, and some chalcedony while pyroxene phenocrysts have opacitic rims; basalt is dark gray, weathering to brown gray; in thin section the basalt has a fine-grained, intergranular texture with plagioclase and clinopyroxene phenocrysts in a groundmass of microlites, glass, and other alteration minerals; plagioclase is replaced by calcite or prehnite, and pyroxene is replaced by clay or iron oxide; groundmass is dark, deeply stained by iron oxides, and includes smectite and other clay minerals; flow-breccia is monolithologic; basal sedimentary interbeds contain abundant feldspar grains, volcanic-derived clasts, and some carbonized

plant fossils; we estimate unit ΦEva$_o$ is up to 2,500 m thick along cross section B–B′; the unit is mapped in the western half of the map area and along the eastern edge of the quadrangle; the flows at the base of unit ΦEva$_o$ appear to interfinger with the underlying Puget Group on the basis of the sedimentary beds. We chose to place the upper contact where flows are less common and overlain by mostly volcaniclastic rocks of unit Φvc$_o$. These rocks were mapped by Tabor and others (2000) as Ohanapecosh Formation and Hammond (1963) as Enumclaw formation. Oligocene plant fossils were found in Coal Creek and the Green River (fossil sites F1 and F2) near the base of this unit by Wolfe (1961, 1968). A new detrital zircon U-Pb maximum depositional age from the bottom of this unit is <35.8 ±0.4 Ma (age site GD1) and a K-Ar age from the upper portion of the section from Phillips (1984) is 33.1 Ma (age site GD4) and suggest unit ΦEva$_o$ is late Eocene to Oligocene.

Early to Middle Eocene Sedimentary Rocks of the Puget Group

Evs$_{pg}$ **Puget Group, undivided (Eocene)**—Coal-bearing sedimentary rocks including feldspathic, micaceous sandstone, carbonaceous siltstone, coal, tuff, and pebble conglomerate; gray to light brown and black, weathering to orange white; sand is fine to coarse; clasts subangular to subrounded; moderately to poorly sorted; sandstone is in tabular beds that are structureless to cross-bedded and siltstone is planar laminated; Vine (1969) estimated a thickness of 1,900 m west of the map area and thicker to the north and south; mapped along the western edge of the quadrangle. The depositional environment of the rocks of the Puget Group represents a terrestrial delta plain upsection of shallow marine strata of the Raging River Formation (Buckovic, 1979; Johnson, 1985; Johnson and O'Connor, 1994). Vine (1969) suggested the unit is derived from the erosion of granitic or metamorphic rocks with the exception of the upper 90 m of section that includes locally derived volcaniclastic sedimentary rock. Hammond (1963) suggested the contact between this unit and overlying rocks (unit ΦEva$_o$) is erosional but Tabor and others (2000) were less certain. The contact between the unit above appears conformable and concordant because both ΦEva$_o$ and Evs$_{pg}$ contain similar feldspathic sandstone to locally derived volcaniclastic sedimentary rock interbedded with carbonaceous plant fossils and have similar dips, suggesting continuous sedimentation in an increasingly volcanic environment. The andesitic, volcaniclastic rocks near the Green River have fission-track and K-Ar ages of approximately 41–45 Ma (Turner and others, 1983). These volcaniclastic rocks likely represent the onset of volcanism from an ancestral Cascade Range based on ages from Tepper and Clark (2024). Walsh and Lingley (1991) found that coal in the deformed Puget Group was first deformed and later thermally matured by Miocene igneous intrusions and metamorphism. The Pocahontas Coal & Coke Co. operated the Big 6 Mine on the western edge of the map area mining coal from this unit in the early 1900s (Washington Geological Survey, 2023a). This unit is Eocene elsewhere in the Puget Lowland (Turner and others, 1983; Wolfe, 1968) and this is consistent with an age of 35.8 Ma (age site GD1) in the overlying unit ΦEva$_o$.

DISCUSSION

Overview of Fault Geometry and Tectonic History

The main faults in the quadrangle, which strike northwest, are the Green River fault and the Piling Creek fault (Hammond, 1963; Tabor and others, 2000). The Green River fault was also called the Lemolo fault by Hammond (1963). Both Hammond (1963) and Tabor and others (2000) mapped the two faults as inferred and Hammond (1963) noted his faults were mapped almost entirely by stratigraphic evidence. We have also mapped them primarily based on stratigraphic considerations and geophysics. While we observed fractures and minor faults near the Green River fault, we did not directly observe the Green River fault or the Piling Creek fault in the field. The Piling Creek fault was mapped by Hammond (1963) as a northwest-striking fault zone with three branches. He suggested the three branches join north of the North Fork Green River and extend to the northwest into the Hobart quadrangle where the fault was mapped by Vine (1962).

The tectonic history of the area includes deformation that spans at least from the Eocene to post-Miocene as evidenced by the oldest rocks—the coal-bearing, Eocene Puget Group—being faulted and tightly folded west of the map area (Willis, 1898; Vine, 1969). The tight folds and faults were recorded in great detail in the coal mines of the area (Willis, 1898; Washington Geological Survey, 2023a) in a way that surficial geologic mapping doesn't allow due to the cover by forests and overburden. According to Walsh and Lingley (1991), the folds in the coal beds of the Puget Group predate the maturation of the coal that likely occurred in the Miocene with intrusion of magma in the area, and this is supported by Warren and others' (1945) interpretation.

On the western edge of the map, the Eocene to Oligocene Ohanapecosh Formation is tilted eastward on top of the Puget Group and the contact between the two appears to be offset in map view by the Green River fault. The tilting is less steep to the east in younger Oligocene andesite flows of the Eagle Gorge (unit Φva$_{eg}$) (see Cross Section B–B′).

In the northeast corner and to the east of the map quadrangle, Hammond (1963) mapped the northwest-trending Lindsay syncline based on structural field observations. This syncline folds both older Ohanapecosh Formation and Eagle Gorge andesites, and the youngest volcanic rocks of the Miocene Fifes Peak Formation as illustrated on the eastern end of Cross Section A–A′ and in the geophysical model (Fig. M1B). The Oligocene Ohanapecosh Formation is thicker than the overlying Miocene Fifes Peak Formation, suggesting more subsidence in the Oligocene than in the Miocene. Further, the Oligocene Ohanapecosh Formation is more folded than Miocene Fifes Peak Formation, indicating

ongoing folding from the Oligocene through the Miocene. These observations suggest that deformation along the Lindsay syncline has been ongoing from the Oligocene through the Miocene.

Mapped Faults

FAULTING ALONG THE GREEN RIVER VALLEY

The Green River fault (Gower and Wanek, 1963), also referred to as the Lemolo fault by Hammond (1963), appears to have offset the north-south-striking contact between the Puget Group and the overlying Ohanapecosh Formation right-laterally in map view. Gower and Wanek (1963) inferred nearly 3,000 ft of right-lateral or 1,400 ft of vertical offset, down to the south to account for this apparent offset, while Hammond (1963) inferred 4,500 ft of horizontal displacement and 8,000 ft of vertical displacement based on offset of the contact between his Eagle Gorge andesite (our unit Ova$_{eg}$) and his Huckleberry Mountain Formation (our unit Ovc$_o$). Gower and Wanek (1963) inferred that a fault observed in coal mines 8 km northwest is a continuation of the Green River fault.

We depict the Green River fault primarily as a right-lateral fault based on the apparent offset of the contacts and geophysical modeling. Though the geophysical modeling suggests a shallowing of basement, thinning of Puget Group, and a slight fold in overlying volcanics at the position of the Green River fault, no vertical offset is required to fit the data (Fig. M1B). A 5 mGal gravity gradient does exist just northeast of the fault, but this is likely sourced by the adjoining ridge, composed of low-density sediment (label VG in Fig. M1A; discussed further below). Farther northwest along the fault, the southwest boundary of a magnetic anomaly likely sourced by volcanic flows (label GRMH in Fig. M1A) is linear, suggesting fault-related truncation of that unit. However, no gravity gradient exists at that location, strongly suggesting no associated vertical offset.

The Green River fault cuts Eocene through Oligocene rocks suggesting that faulting along the Green River fault occurred after the Oligocene. The fault projects to the east into the Cougar Mountain quadrangle where it may bound a block of folded, Miocene andesite (Tabor and others, 2000).

A minor shear zone downstream of Howard A. Hanson Dam south of the Green River fault in the Green River valley is oriented east-west, and is thus likely not a part of the northwest-southeast-oriented Green River fault. This shear zone is covered with alpine drift, but the alpine drift does not appear deformed or faulted. The lack of faulting in the alpine drift suggests that the minor shear zone fault has not ruptured at the surface since at least the Fraser glaciation.

PILING CREEK FAULT

Hammond (1963) mapped a 24-km-long fault in the North Fork Green River valley which he described as a branching fault zone that continues northwest to the Hobart fault of Vine (1962). The Piling Creek fault uplifts the block we map as unit OEva$_o$ along the eastern boundary of the map area.

We choose not to map a continuous fault for two reasons: (1) our estimates for unit thickness along cross section A–A′ do not require faulting; and (2) a fault is not required to fit the geophysical data at the location in the North Fork Green River valley where Hammond's (1963) mapped fault should cross our geophysical model and cross section. There is a small misfit between the model prediction and the magnetic data (see label MMF2 in Fig. M1B) at this location, so a fault here could be permissible, but there are not enough gravity and magnetic data points to provide a conclusive interpretation of a fault here.We do find good evidence for additional faulting to the northeast of the Piling Creek fault, including multiple northwest-striking, high-angle, north-side-down faults between Piling Creek and the North Fork Green River and in the valley of the South Fork Taylor Creek. These faults are also supported by an increase in dip of strata along cross section A–A′ near the South Fork Taylor Creek. Abrupt changes in thicknesses of near-surface, magnetic units across one fault required to model the magnetic data and a spatially correlated gravity gradient (see label SG1 in Fig. M1A and B) support at least one of these strands crossing the cross section (see *Lindsay syncline and associated faults*).

FAULTING AND FOLDING IN THE NORTHEAST CORNER OF THE MAP AREA

Our field observations indicate that the Miocene Fifes Peak Formation (unit Mva$_{fp}$) has been tightly folded and faulted into a syncline that Hammond (1963) mapped as the Lindsay syncline. Geophysics also suggest faulting and folding in this area. Colocated, curvilinear, steep gravity and magnetic gradients (see label SG2 and FMG in Fig. M1A and B) are best fit with near-vertical faults (see *Lindsay syncline and associated faults*) with an apparent offset of younger volcanics (unit Mva$_{fp}$) into a folded basin. Together, these field observations and geophysical modeling suggest a tightly folded syncline and a northwest-trending, inferred fault northeast of the syncline.

Geophysical Evidence for Subsurface Structures

We present a combined isostatic gravity and aeromagnetic geophysical anomaly map (Fig. M1A) and a geophysical model (Fig. M1B) that support our interpretations in the geologic map and cross section. The geophysical model is contiguous with a similar model constructed for the Chester Morse Lake 7.5-minute quadrangle geologic map (Steely and others, 2022), and rock lithologies and structures identified from that work continue into this section.

GEOPHYSICAL CONTROL ON STRUCTURAL GEOMETRIES

The modeled geophysical anomalies are sensitive to relative changes in depth of the top of basement (here, the western mélange belt; Anderson and others, 2024). These anomalies also distinguish denser and more magnetic flows and intrusions from less dense and less magnetic volcaniclastic layers (tuff, breccia, conglomerate, sedimentary) in the Neogene volcanic and sedimentary strata. Thus, the geophysical anomalies constrain three subsurface vertical or dipping contact geometries very well: volcanic strata, faults disrupting such strata, and intrusion lateral boundaries. The strongest constraints on these details are in the upper 3 km of the subsurface strata. Though geophysical data respond to local relative changes in basement depth, we use consistent basement density and magnetic properties across the

model because potential variation in composition makes absolute depth of the top of basement uncertain.

NEOGENE VOLCANIC STRATA

Many of the ridges in the map area are entirely composed of low-density deposits such as volcaniclastic material (less than the 2,670 kg/m^3 reduction density used for computing geophysical anomalies), thus creating gravity gradients associated with hillslopes that decrease upslope and increase downslope. See for example the gravity gradient associated with volcaniclastics, label VG in Fig. M1A and B, which disappears to the northwest where the ridge is filled with denser, more magnetic flows (see label GRMH in Fig. M1A and B). If such a topographically controlled gradient disappears in map view without a commensurate change in topography, it signifies that the lithology composing the ridge has changed to be closer to the reduction density. Such gradient changes help confirm the location of contacts between units that are predominantly volcaniclastic and units dominated by volcanic flows, but obscure gravitational features arising from other sources such as faults. There is little to no difference in either density or magnetism between volcanic stratigraphy of different ages (Data Supplement), therefore we are unable to interpret the age of a subsurface unit from geophysical data. Though units are assigned an age in the geophysical model, this is inferred from the geologic mapping. Many of the shorter-wavelength (1–2 km) anomalies in both magnetics and gravity can be easily fit by steeply (>30 degree) dipping stratigraphy, especially across the center and northern section of the map (see label DB in Fig. M1A and B), consistent with geological unit dips at the surface.

BASEMENT INTRUSION

A long-wavelength (~30 km) magnetic anomaly high spans most of X–X′ (label LMH in Fig. M1B marks its northeastern edge, and the anomaly continues off the line to the southwest). This anomaly could result from an Eocene or younger intrusion at depth, or from a large wedge of gabbro within the Jurassic-Cretaceous western mélange belt (similar to wedges of gabbro mapped to the north of this quadrangle (Dragovich and others, 2015; Steely and others, 2022)). We have modeled the magnetic source with a 30-km-wide, 5-km-deep intrusion of rock with properties that most closely fit diorite (this intrusion is too deep to appear on the model). However, if there is additional material at depth (>3 km) that is denser than modeled basement or this intrusion, the top of basement could be deeper than shown in Fig. M1B. Therefore, the depth of the contact between the dipping beds and the basement (UC in Fig. M1B) remains uncertain. The basement–Neogene volcanics contact could be deeper, and thus accommodate slightly more simple or complex geometry of volcanic rock just above the contact.

SHALLOW INTRUSIONS

High-amplitude, shorter-wavelength (~1.5 km) aeromagnetic anomalies in the southwest portion of the map area (see for example anomalies labeled IMH in Fig. M1A and B) cannot be modeled by shallow flows, especially due to the apparent shallow dip of units in this region. These anomalies are also not elongated along bedding strike in map view and have irregular bounding gradients. These observations suggest that these anomalies are not related to bedding as mapped and intrusions are the most logical source of these anomalies. These inferred intrusions appear on the geophysical model, but not on the geologic cross section, because the only evidence of their existence is geophysical data. However, previous mapping (Hammond, 1963) shows small, local intrusions 4 km south of the quadrangle, which gives a regional plausibility to this hypothesis. As noted above, we have also modeled a larger intrusion >5 km depth under the map area, which suggests a source for such shallower intrusions. The density and magnetic properties needed for these shallow intrusions (2,640 kg/m^3 and 48 x 10^{-3} SI) are similar to the larger, deeper modeled intrusion and mapped dioritic lithologies (Hammond, 1963). As such, we accept slight misfit between our model and magnetic data (see locations labeled MMF in Fig. M1B), which may also be due to small, local intrusions that are too small to resolve with our data (or other unresolvable geologic features).

LINDSAY SYNCLINE AND ASSOCIATED FAULTS

A prominent gravity low (SGL in Fig. M1A and B) marks a ~5-km-deep basin, the main structural feature detailed by the geophysical data. This basin contains a geologically mapped syncline, which is also included in the geophysical model. We hypothesize that the basin and syncline are genetically related. Linear gravity gradients on either side of the gravity low delineate the edges of the basin (SG1 and SG2 in Fig. M1A and B). Attempts to shallow the dip of the boundaries sourcing these gravity gradients while honoring the surface geology only allow an 80 degree dip at a minimum, particularly on the northeast boundary of the syncline (SG2 in Fig. M1). We are confident interpreting this northeast boundary as a fault, in terms of both its location and geometry. The first line of supporting evidence is the high magnetic gradient northeast of label MHF in Fig. M1B combined with moderate bedding dips observed at the surface, which can only be interpreted and modeled with a magnetic flow that is truncated. The second line of evidence is the colocated steep gravitational gradient labeled ‘SG2’ in Fig. M1B that is most reasonably fit by a ~2 km offset on the top of basement. The third is that the youngest unit (Mva$_{fp}$) is more steeply dipping than the older unit (Ova$_{eg}$) across this fault. The location of the other faults within the basin and bounding it to the southwest are strongly supported by the linearity of short-wavelength gravity and magnetic gradients such as those at SG1 and FMG in Fig. M1B. However, the exact dips of these structures are less certain. The resulting geometry from our fault interpretations suggests the basin is fault bounded; a transtensional origin would fit the implied style of faulting. The geologic observations of more steeply dipping younger rocks near less steeply dipping older rocks in a tight syncline less than 150 m wide support the syncline and suggest faulting at the edges, especially along gradient SG2. A longer-wavelength (5 km) magnetic high over the basin (SMH in Fig. M1B), combined with the gravity low suggests that the basin is filled with low-density, slightly magnetic volcanic material, either volcaniclastic rocks or sediment with a volcanic provenance, layered with more-magnetic flows. The geometry, thickness, and physical properties of layers deeper than ~1,200 m below the surface in the basin are unclear and inferred by exposed, older layers of Eocene volcanic rocks southwest and northeast of the basin. The age of the faulting is

unclear. The geophysical data could be consistent with growth strata within the basin, indicating at least some of its formation is Eocene–Miocene in age, but that is far from certain given stratigraphy deeper within the basin is hard to constrain with the geophysics. Tight folding of mapped Miocene strata suggests significant post-Miocene deformation. But this deformation would be consistent with compression or transpression rather than transtension. The geophysical properties of the volcanic rocks are complex enough to potentially hide small offsets along faults with younger movement.

CONCLUSIONS

The combination of field observations, geophysical data, and subsurface modeling helped delineate and interpret the larger folds and faults in the map area and shed new insights into these structures, including:

- The Green River fault was previously inferred but the geometry was uncertain. Here, both the geophysics and geologic mapping suggest this fault is a right-lateral fault based both on the apparent right-lateral offset of the contact between the Puget Group and the Ohanapecosh Formation, and the geophysical modeling suggesting that there is no apparent vertical offset in the basement rocks.

- The Piling Creek fault doesn't appear to be one major northwest-striking fault because the geophysics doesn't directly support vertical offset of basement bedrock, geologic mapping at the surface doesn't suggest lateral offset of units, and the cross section interpretation does not show that the units are thicker beyond what is estimated for unit thickness in the area. The Piling Creek fault may instead consist of multiple faults along the eastern portion of the map area. Uplift along such faults would explain an uplifted block of Ohanapecosh andesite flows observed in the area (unit Eva_{O}).

- Faulting near the Lindsay syncline, in the northeast corner of the map, is supported by both geophysics and geologic mapping observations. The deformation associated with the Lindsay syncline appears to have been ongoing through time, forming a synclinal basin that formed and filled with volcaniclastic sediment and flows through the Oligocene and Miocene. The deformation of the area continued at least into post-Miocene time with folding of the Miocene Fifes Peak Formation and development of the inferred faults.

- Northwest-trending scarps that are observed in lidar near the northeast corner of the map area are on trend with one of the inferred faults, but the scarps occur in landslide deposits, making it difficult to tell whether the scarps are fault or landslide related. That uncertainty, combined with the geologically complex faulting and steeply tilting andesite flows and flow breccia in the area, led us to not map these scarps as surface-rupturing faults.

ACKNOWLEDGMENTS

We thank Alex Steely for an introduction to and insight into the map area; Alex Steely, Michael Polenz, and Andrew Sadowski for helpful reviews; Alex Steely for the GeMS database template and collecting data in Field Maps; Tim Walsh (WGS retired) for a thoughtful review and addressing questions about prior mapping; Daniel Coe, Joel Gombiner, Nikolas Midttun, and Susan Schnur for drafting figures and editing along with all WGS staff who provided suggestions, edits, and guidance; City of Tacoma and City of Seattle employees who assisted with access to the area, especially Carol at the gatehouse; the US Army Corps of Engineers including Sharon Gelinas for information about the Howard A. Hanson Dam; and countless other landowners for land access and local knowledge.

AUTHOR CONTRIBUTIONS

M. Anderson provided geophysical modeling and writing pertaining to the geophysical work. A. Bauer collected gravity data and assessed rock density and magnetic susceptibility for input into the geophysical model. A. Lockett carried out geologic fieldwork and mapping of primarily bedrock units, constructed the A–A′ cross section, examined thin sections, and wrote portions of the bedrock unit descriptions. T. Contreras functioned as project lead, led geologic fieldwork, and drafted GIS features and the report.

REFERENCES

Ali, Arfan; Potter, D. K.; Tugwell, Andrew, 2015, Magnetic susceptibility of drill cuttings in a North Sea oil well: A rapid, nondestructive means of characterizing lithology: 2015 International Symposium of the Society of Core Analysts, St. John's, Newfoundland and Labrador, Canada, Paper SCA2015-036, 6 p. [https://www.jgmaas.com/SCA/2015/SCA2015-036.pdf]

Anderson, M. L.; Blakely, R. J.; Wells, R. E.; Dragovich, J. D., 2024, Deep structure of Siletzia in the Puget Lowland: Imaging an obducted plateau and accretionary thrust belt with potential fields: Tectonics, v. 43, no. 2, e2022TC007720. [https://doi.org/10.1029/2022TC007720]

Armstrong, J. E.; Crandell, D. R.; Easterbrook, D. J.; Noble, J. B., 1965, Late Pleistocene stratigraphy and chronology in southwestern British Columbia and northwestern Washington: Geological Society of America Bulletin, v. 76, no. 3, p. 321–330. [https://doi.org/10.1130/0016-7606(1965)76[321:LPSACI]2.0.CO;2]

Barnes, D. F.; Oliver, H. W.; Robbins, S. L., 1969, Standardization of gravimeter calibrations in the Geological Survey: Eos Transactions, v. 50, no. 10, p. 626–627. [https://doi.org/10.1029/EO050i010p00526]

Barnett, E. A.; Haugerud, R. A.; Sherrod, B. L.; Weaver, C. S.; Pratt, T. L.; Blakely, R. J., compilers, 2010, Preliminary atlas of active shallow tectonic deformation in the Puget Lowland, Washington: U.S. Geological Survey Open-File Report 2010–1149, 32 p., 14 maps. [https://pubs.usgs.gov/of/2010/1149/]

Beikman, H. M.; Gower, H. D.; Dana, T. A. M.; with addendum by Schasse, H. W.; Walsh, T. J.; Phillips, W. M., 1961, repr. with addendum 1984, Coal reserves of Washington: Washington Division of Geology and Earth Resources Bulletin 47, 134 p. [https://www.dnr.wa.gov/Publications/ger_b47_coal_reserves_wa.pdf]

Berggren, W. A.; Kent, D. V.; Flynn, J. J.; Van Couvering, J. A., 1985, Cenozoic geochronology: Geological Society of America Bulletin, v. 96, no. 11, p. 1407–1418. [https://doi.org/10.1130/0016-7606(1985)96%3C1407:CG%3E2.0.CO;2]

Berggren, W. A.; Kent, D. V.; Swisher, C. C.; Aubry, M.-P., 1995, A revised Cenozoic geochronology and chronostratigraphy. *In* Berggren, W. A.; Kent, D. V.; Hardenbol, Jan, editors, Geochronology, time scales and global stratigraphic correlation: SEPM (Society for Sedimentary Geology) Special Publication 54, p. 129–212. [https://doi.org/10.2110/pec.95.04.0129]

Black, B. A.; Pearl, J. K.; Pearson, C. L.; Pringle, P. T.; Frank, D. C.; Page, M. T.; Buckley, B. M.; Cook, E. R.; Harley, G. L.; King, K. J.; Hughes, J. F.; Reynolds, D. J.; Sherrod, B. L., 2023, A multifault earthquake threat for the Seattle metropolitan region revealed by mass tree mortality: Science Advances, v. 9, no. 39. [https://doi.org/10.1126/sciadv.adh4973]

Black, L. P.; Kamo, S. L.; Allen, C. M.; Davis, D. W.; Aleinikoff, J. N.; Valley, J. W.; Mundil, Roland; Campbell, I. H.; Korsch, R. J.; Williams, I. S.; Foudoulis, Chris, 2004, Improved $^{206}Pb/^{238}U$ microprobe geochronology by the monitoring of a trace-element-related matrix effect; SHRIMP, ID-TIMS, ELA-ICP-MS and oxygen isotope documentation for a series of zircon standards: Chemical Geology, v. 205, p. 115–140. [https://doi.org/10.1016/j.chemgeo.2004.01.003]

Blakely, R. J.; Wells, R. E.; Weaver, C. S., 1999, Puget Sound aeromagnetic maps and data: U.S. Geological Survey Open-File Report 99-514, version 1.0. [https://doi.org/10.3133/ofr99514]

Booth, D. B., 1986, The formation of ice-marginal embankments into ice-dammed lakes in the eastern Puget Lowland, Washington, USA, during the late Pleistocene: Boreas, v. 15, no. 3, p. 209–264. [https://doi.org/10.1111/j.1502-3885.1986.tb00929.x]

Booth, D. B., 1990, Surficial geologic map of the Skykomish and Snoqualmie Rivers area, Snohomish and King counties, Washington: U.S. Geological Survey Miscellaneous Investigations Series Map I-1745, 2 sheets, scale 1:50,000, 22 p. text. [https://doi.org/10.3133/i1745]

Bretz, JH, 1913, Glaciation of the Puget Sound Region: Washington Geological Survey Bulletin 8, 244 p., 3 plates. [http://www.dnr.wa.gov/publications/ger_b8_glaciation_pugetsound.pdf]

Brocher, T. M.; Parsons, T. E.; Blakely, R. J.; Christensen, N. I.; Fisher, M. A.; Wells, R. E., 2001, Upper crustal structure in Puget Lowland, Washington: Results from the 1998 Seismic Hazards Investigations in Puget Sound: Journal of Geophysical Research Solid Earth, v. 106, no. B7, p. 13,541–13,564. [https://doi.org/10.1029/2001JB000154]

Buckovic, W. A., 1979, The Eocene Deltaic System of West-Central Washington. *In* Armentrout, J. M.; Cole, M. R.; Ter Best, Harry, Jr., editors, Cenozoic Paleogeography of the Western United States: Society of Economic Paleontologists and Mineralogists Pacific Section, Pacific Coast Paleogeography Symposium 3, p. 147–163. [https://archives.datapages.com/data/pac_sepm/024/024001/pdfs/147.htm]

Chang, Zhaoshan; Vervoort, J. D.; McClelland, W. C.; Knaack, Charles, 2006, U-Pb dating of zircon by LA-ICP-MS: Geochemistry, Geophysics, Geosystems, v. 7, p. Q05009. [https://doi.org/10.1029/2005GC001100]

Crandell, D. R., 1963, Surficial geology and geomorphology of the Lake Tapps quadrangle, Washington: U.S. Geological Survey Professional Paper 388-A, 84 p., 2 plates. [https://doi.org/10.3133/pp388A]

Crandell, D. R.; Miller, R. D., 1974, Quaternary stratigraphy and extent of glaciation in the Mount Rainier region, Washington: U.S. Geological Survey Professional Paper 847, 59 p., 2 plates. [https://doi.org/10.3133/pp847]

DirectAMS, 2023, Radiocarbon dating wood, plant, & cellulose [webpage]: DirectAMS Radiocarbon Dating Service. [accessed Jun. 12, 2023, at https://www.directams.com/wood-plant-cellulose]

Dragovich, J. D.; Anderson, M. L.; Walsh, T. J.; Johnson, B. L.; Adams, T. L., 2007, Geologic map of the Fall City 7.5-minute quadrangle, King County, Washington: Washington Division of Geology and Earth Resources Geologic Map GM-67, 1 sheet, scale 1:24,000. [https://www.dnr.wa.gov/Publications/ger_gm67_geol_map_fallcity_24k.zip]

Dragovich, J. D.; Walsh, T. J.; Anderson, M. L.; Hartog, Renate; DuFrane, S. A.; Vervoot, Jeff; Williams, S. A.; Cakir, Recep; Stanton, K. D.; Wolff, F. E.; Norman, D. K.; Czajkowski, J. L., 2009, Geologic map of the North Bend 7.5-minute quadrangle, King County, Washington, with a discussion of major faults, folds, and basins in the map area: Washington Division of Geology and Earth Resources Geologic Map GM-73, 1 sheet, scale 1:24,000, with 39 p. text. [https://www.dnr.wa.gov/Publications/ger_gm73_geol_map_northbend_24k.zip]

Dragovich, J. D.; Mahan, S. A.; Anderson, M. L.; MacDonald, J. H., Jr; Schilter, J. F.; Frattali, C. L.; Koger, C. J.; Smith, D. T.; Stoker, B. A.; DuFrane, Andrew; Eddy, M. P.; Cakir, Recep; Sauer, K. B., 2015, Geologic map of the Lake Roesiger 7.5-minute quadrangle, Snohomish County, Washington: Washington Division of Geology and Earth Resources Map Series 2015-01, 1 sheet, scale 1:24,000, with 47 p. text. [https://www.dnr.wa.gov/publications/ger_ms2015-01_geol_map_lake_roesiger_24k.zip]

Finn, C. A.; Phillips, W. M.; Williams, D. L., 1991, Gravity anomaly and terrain maps of Washington: U.S. Geological Survey Geophysical Investigations Map 988, 5 plates, scale 1:500,000. [https://doi.org/10.3133/gp988]

Fiske, R. S., 1963, Subaqueous pyroclastic flows in the Ohanapecosh Formation, Washington: Geological Society of America Bulletin, v. 74, no. 4, p. 391–406. [https://doi.org/10.1130/0016-7606(1963)74[391:SPFITO]2.0.CO;2]

Gaschnig, R. M.; Vervoort, J. D.; Lewis, R. S.; McClelland, W. C., 2010, Migrating magmatism in the northern US Cordillera: in situ U-Pb geochronology of the Idaho batholith: Contributions to Mineralogy and Petrology, v. 159, p. 863–883. [https://doi.org/10.1007/s00410-009-0459-5]

Gower, H. D.; Wanek, A. A., 1963, Preliminary geologic map of the Cumberland quadrangle, King County, Washington: Washington Division of Mines and Geology Geologic Map GM-2, 1 sheet, scale 1:24,000. [https://www.dnr.wa.gov/Publications/ger_gm2_geol_map_cumberland_24k.pdf]

Hammond, P. E., 1963, Structure and stratigraphy of the Keechelus Volcanic Group and associated Tertiary rocks in the west-central Cascade Range, Washington: University of Washington Doctor of Philosophy thesis, 254 p., 2 plates. [https://www.proquest.com/openview/e4da8a30c5ed36d276f71a96327db1f7/1?pq-origsite=gscholar&cbl=18750&diss=y]

Hammond, P. E.; Dragovich, J. D., 2008, Tuff of Stampede Pass and tuff of Green Canyon in the central Cascade Range, King and Kittitas Counties, Washington: Washington Division of Geology and Earth Resources Open File Report 2008-3, 8 p. text with 1 Excel file on DVD. [https://www.dnr.wa.gov/Publications/ger_ofr2008-3_stampedepass_greencanyon_tuff.zip]

Hartman, D. A., 1973, Geology and Low-Grade Metamorphism of the Greenwater River Area, Central Cascade Range, Washington: University of Washington Doctor of Philosophy thesis, 99 p., 2 plates. [https://www.proquest.com/openview/a16185eee64f7fde3f6c894c03000f57/1?pq-origsite=gscholar&cbl=18750&diss=y]

Haugerud, R. A., 2021, Deglaciation of the Puget Lowland, Washington. *In* Waitt, R. B.; Thackray, G. D.; Gillespie, A. R., editors, Untangling the Quaternary Period—A Legacy of Stephen C. Porter: Geological Society of America Special Paper 548, p. 279–298. [https://doi.org/10.1130/2020.2548(14)]

Heiskanen, W. A.; Vening-Meinesz, F. A., 1958, The Earth and its gravity field: McGraw-Hill Book Company, Inc., 470 p. [https://doi.org/10.1126/science.129.3347.460.b]

International Association of Geodesy and Geophysics, 1971, Geodetic reference system 1967: International Association of Geodesy Special Publication No. 3, 116 p.

Johnson, S. Y.; O'Connor, J. T., 1994, Stratigraphy, sedimentology, and provenance of the Raging River Formation (early? and middle Eocene), King County, Washington: U.S. Geological Survey Bulletin 2085-A, 33 p. [https://doi.org/10.3133/b2085A]

Johnson, S. Y., 1985, Eocene strike-slip faulting and nonmarine basin formation in Washington. *In* Biddle, K. T.; Christie-Blick, Nicholas, editors, Strike-slip deformation, basin formation, and sedimentation: Society of Economic Paleontologists and Mineralogists Special Publication 37, p. 283–302. [https://archives.datapages.com/data/sepm_sp/SP37/Eocene_Strike_Slip_Faulting.htm]

Johnson, S. Y.; Dadisman, S. V.; Childs, J. R.; Stanley, W. D., 1999, Active tectonics of the Seattle fault and central Puget Sound, Washington—Implications for earthquake hazards: Geological Society of America Bulletin, v. 111, no. 7, p. 1042–1053, 1 plate. [https://doi.org/10.1130/0016-7606(1999)111%3C1042:ATOTSF%3E2.3.CO;2]

Lanphere, M A.; Baadsgaard, Halfdan, 2001, Precise K–Ar, $^{40}Ar/^{39}Ar$, Rb–Sr and U/Pb mineral ages from the 27.5 Ma Fish Canyon Tuff reference standard: Chemical Geology, vol. 175, issues 3–4. [https://doi.org/10.1016/S0009-2541(00)00291-6]

Ludwig, K. R., 2003, Isoplot 3.00: A geochronological toolkit for Microsoft Excel: Berkeley Geochronology Center, Berkeley, 70 p.

Mackin, J. H., 1941, Glacial Geology of the Snoqualmie-Cedar Area, Washington: Journal of Geology, v. 49, no. 5, p. 449–481. [https://doi.org/10.1086/624984]

Mickelson, K. A.; Jacobacci, K. E.; Contreras, T. A.; Gallin, W. N.; Slaughter, S. L., 2019, Landslide inventory of western King County, Washington: Washington Geological Survey Report of Investigations 41, 7 p. text, with an accompanying Esri file geodatabase. [https://fortress.wa.gov/dnr/geologydata/publications/ger_ri41_western_king_county_landslide_inventory.zip]

Morelli, Carlo, editor, 1974, The international gravity standardization net 1971: International Association of Geodesy Special Publication No. 4, 194 p.

Nelson, A. R.; Personius, S. F.; Sherrod, B. L.; Buck, Jason; Bradley, Lee-Ann; Henley, Gary, II; Liberty, L. M.; Kelsey, H. M.; Witter, R. C.; Koehler, R. D.; Schermer, E. R.; Nemser, E. S.; Cladouhos, T. T., 2008, Field and laboratory data from an earthquake history study of scarps in the hanging wall of the Tacoma fault, Mason and Pierce Counties, Washington: U.S. Geological Survey Scientific Investigations Map 3060, 3 sheets, scale 1:30,000. [https://pubs.usgs.gov/sim/3060/]

Noble, J. B.; 1969, Geohydrologic investigation of the North Fork of Green River valley: Robinson, Roberts & Associates, Inc., 29 p.

Paces, J. B.; Miller, J. D., Jr., 1993, Precise U-Pb ages of Duluth Complex and related mafic intrusions, northeastern Minnesota: Geochronological insights to physical, petrogenetic, paleomagnetic, and tectonomagmatic processes associated with the 1.1 Ga Midcontinent Rift System: Journal of Geophysical Research Solid Earth, v. 98, p. 13,997–14,013. [https://doi.org/10.1029/93JB01159]

Paton, Chad; Hellstrom, John; Paul, Bence; Woodhead, Jon; Hergt, Janet, 2011, Iolite: Freeware for the visualisation and processing of mass spectrometric data: Journal of Analytical Atomic Spectrometry, v. 26, p. 2508–2518. [https://doi.org/10.1039/C1JA10172B]

Phillips, W. M., 1984, Compilation geologic map of the Green River coal district, King County, Washington: Washington Division of Geology and Earth Resources Open File Report 84-4, 4 p., 3 plates. [https://www.dnr.wa.gov/Publications/ger_ofr84-4_green_river_coal_district_24k.pdf]

Phillips, J. D.; Hansen, R. O.; Blakely, R. J., 2007, The use of curvature in potential-field interpretation: Exploration Geophysics, v. 38, no. 2, p. 111–119. [https://doi.org/10.1071/EG07014]

Plouff, Donald, 2000, Field estimates of gravity terrain corrections and Y2K-compatible method to convert from gravity readings with multiple base stations to tide-and long-term drift-corrected observations: U.S. Geological Survey Open-File Report OF 00-140, 35 p. [https://doi.org/10.3133/ofr00140]

Polenz, Michael; Hladky, F. R.; Bauer, A. L.; Lau, T. R.; Tepper, J. H.; Nesbitt, E. A.; Legorreta Paulín, Gabriel, 2023, Geologic map of the Bald Hill 7.5-minute quadrangle, Thurston, Pierce, and Lewis Counties, Washington: Washington Geological Survey Map Series 2023-03, 1 sheet, scale 1:24,000, with 37 p. text. [https://www.dnr.wa.gov/publications/ger_ms2023-03_geol_map_bald_hill_24k.zip]

Polenz, Michael; Hladky, F. R.; Anderson, M. L.; Alexander, K. A.; Tepper, J. H.; Miggins, D. P.; Legoretta Paulin, Gabriel, 2022, Geologic map of the McKenna and northern half of the Lake Lawrence 7.5-minute quadrangles, Thurston and Pierce Counties, Washington: Washington Geological Survey Map Series 2022-06, 1 sheet, scale 1:24,000, 35 p. text. [https://www.dnr.wa.gov/publications/ger_ms2022-06_geol_map_mckenna_northern_lake_lawrence_24k.zip]

Polenz, Michael; Hladky, F. R.; Anderson, M. L.; Tepper, J. H.; Horst, A. E.; Miggins, D. P.; Legoretta Paulín, Gabriel, 2021, Geologic map of the Tenalquot Prairie and northern two-thirds of the Vail 7.5-minute quadrangles, Thurston and Pierce Counties, Washington: Washington Geological Survey Map Series 2021-02, 1 sheet, scale 1:24,000, 47 p. text. [https://www.dnr.wa.gov/publications/ger_ms2021-02_geol_map_tenalquot_prairie_northern_vail_24k.zip]

Polenz, Michael; Ostrom, B. A.; Lau, T. R.; Sadowski, A. J.; Blanks-Bennett, A. L.; Cakir, Recep; Tepper, J. H.; Legoretta Paulín, Gabriel; Nesbitt, Elizabeth; DuFrane, S. A., 2018, Geologic map of the Violet Prairie 7.5-minute quadrangle, Thurston and Lewis Counties, Washington: Washington Geological Survey Map Series 2018-04, 1 sheet, scale 1:24,000, 41 p. text. [https://www.dnr.wa.gov/publications/ger_ms2018-04_geol_map_violet_prairie_24k.zip]

Polenz, Michael; Favia, J. G.; Hubert, I. J.; Legorreta Paulín, Gabriel; Cakir, Recep, 2015, Geologic map of the Port Ludlow and southern half of the Hansville 7.5-minute quadrangles, Kitsap and Jefferson Counties, Washington: Washington Division of Geology and Earth Resources Map Series 2015-02, 1 sheet, scale 1:24,000, with 40 p. text. [https://www.dnr.wa.gov/publications/ger_ms2015-02_geol_map_port_ludlow_hansville_24k.zip]

Porter, S. C.; Swanson, T. W., 1998, Radiocarbon age constraints on rates of advance and retreat of the Puget lobe of the Cordilleran ice sheet during the last glaciation: Quaternary Research, v. 50, no. 3, p. 205–213. [https://doi.org/10.1006/qres.1998.2004]

Porter, S. C., 1976, Pleistocene glaciation in the southern part of the north Cascade Range, Washington: Geological Society of America Bulletin, v. 87, no. 1, p. 61–75. [https://doi.org/10.1130/0016-7606(1976)87<61:PGITSP>2.0.CO;2]

Sherrod, B. L.; Blakely, R. J.; Weaver, C. S.; Kelsey, H. M.; Barnett, Elizabeth; Liberty, Lee; Meagher, K. L.; Pape, Kristin, 2008, Finding concealed active faults: Extending the southern Whidbey Island fault across the Puget Lowland, Washington: Journal of Geophysical Research: Solid Earth, v. 113, no. B5. [https://doi.org/10.1029/2007JB005060]

Sláma, Jiří; Košler, Jan; Condon, D. J.; Crowley, J. L.; Gerdes, Axel; Hanchar, J. M.; Horstwood, M. S. A.; Morris, G. A.; Nasdala, Lutz; Norberg, Nicholas; Schaltegger, Urs; Schoene, Blair; Tubrett, M. N.; Whitehouse, M. J., 2008, Plešovice zircon—A new natural reference material for U-Pb and Hf isotopic microanalysis: Chemical Geology, v. 249, no. 1-2, p. 1–35. [https://doi.org/10.1016/j.chemgeo.2007.11.005]

Smith, G. O.; Calkins, F. C., 1906, Geologic atlas of the United States—Snoqualmie folio, Washington: U.S. Geological Survey Geologic Folio 139, 14 p., 3 sheets, scale 1:125,000. [https://doi.org/10.3133/gf139]

Steely, A. N.; Anderson, M. L.; Alexander, K. A., 2022, Geologic map of the Chester Morse Lake 7.5-minute quadrangle, King County, Washington: Washington Geological Survey Map Series 2022-04, 1 sheet, scale 1:24,000, 33 p. text. [https://www.dnr.wa.gov/publications/ger_ms2022-04_geol_map_chester_morse_lake_24k.zip]

Swick, C. H., 1942, Pendulum gravity measurements and isostatic reductions: U.S. Coast and Geodetic Survey Special Publication No. 232, 82 p.

Tabor, R. W.; Frizzell, V. A., Jr.; Booth, D. B.; Waitt, R. B., 2000, Geologic map of the Snoqualmie Pass 30 x 60 minute quadrangle, Washington: U.S. Geological Survey Geologic Investigations Series Map I-2538, 1 sheet, scale 1:100,000, with 57 p. text. [https://pubs.usgs.gov/imap/i2538/]

Tacoma Public Utilities, 2024, The Green River municipal watershed [webpage]: Tacoma Public Utilities. [accessed Jun. 12, 2024, at https://www.mytpu.org/about-tpu/services/water/water-source/green-river-watershed/]

Telford, W. M.; Geldart, L. P.; Sheriff, R. E., 1990, Applied Geophysics. Cambridge University Press, 770 p.

Tepper, J. H.; Clark, K. P., 2024, Initiation of the Cascade arc: Geology, v. 52, no. 4, p. 297–301. [https://doi.org/10.1130/G51888.1]

Turner, D. L.; Frizzell, V. A., Jr.; Triplehorn, D. M.; Naeser, C. W., 1983, Radiometric dating of ash partings in coals of the Eocene Puget Group, Washington: Implications for paleobotanical stages: Geology, v. 11, no. 9, p. 527–531. [https://doi.org/10.1130/0091-7613(1983)11<527:RDOAPI>2.0.CO;2]

Vine, J. D., 1962, Preliminary geologic map of the Hobart and Maple Valley quadrangles, King County, Washington: Washington Division of Mines and Geology Geologic Map GM-1, 1 sheet, scale 1:24,000. [https://www.dnr.wa.gov/Publications/ger_gm1_geol_map_hobartmaplevalley_24k.pdf]

Vine, J. D., 1969, Geology and coal resources of the Cumberland, Hobart, and Maple Valley quadrangles, King County, Washington: U.S. Geological Survey Professional Paper 624, 67 p., 4 plates. [https://doi.org/10.3133/pp624]

Waitt, R. B.; Thorson, R. M., 1983, The Cordilleran ice sheet in Washington, Idaho, and Montana. *In* Porter, S. C.; Wright, H. E., Jr., editors, Late-Quaternary environments of the United States: University of Minnesota Press, p. 53–70.

Walker, J. D.; Geissman, J. W., compilers, 2022, Geologic Time Scale v. 6.0: Geological Society of America. [https://doi.org/10.1130/2022.CTS006C]

Walsh, T. J.; Lingley, W. S., Jr., 1991, Coal maturation and the natural gas potential of western and central Washington: Washington Division of Geology and Earth Resources Open File Report 91-2, 26 p. [https://www.dnr.wa.gov/publications/ger_ofr91-2_coal_maturation_gas_potential.pdf]

Walsh, T. J., 1984, Geology and coal resources of central King County, Washington: Washington Division of Geology and Earth Resources Open File Report 84-3, 24 p., 2 plates. [https://www.dnr.wa.gov/Publications/ger_ofr84-3_central_king_co_coal_24k.pdf]

Warren, W. C.; Norbisrath, Hans; Grivetti, R. M.; Brown, S. P., 1945, Preliminary geologic map and brief description of the coal fields of King County, Washington: U.S. Geological Survey Preliminary Map, 1 sheet, scale 1:31,680.

Washington Geological Survey, 2022, King County East 2021 project [lidar data]: originally contracted by Washington Dept. of Natural Resources and U.S. Geological Survey. [accessed Jun. 22, 2023, at https://lidarportal.dnr.wa.gov]

Washington Geological Survey, 2024, Geothermal Wells—GIS Data: Washington Geological Survey Digital Data Series 8, version 2.1, previously published October 2014. [https://fortress.wa.gov/dnr/geologydata/publications/data_download/ger_portal_geothermal_wells.zip]

Washington Geological Survey, 2023a, Mines and Minerals—GIS data: Washington Geological Survey Digital Data Series 30, version 2.0, previously published January 2023. [https://fortress.wa.gov/dnr/geologydata/publications/data_download/ger_portal_mines_minerals.zip]

Washington Geological Survey, 2023b, Gravity Base Station Data, Geophysics Database—GIS data: Washington Geological Survey Digital Data Series 28, version 1.0, April 2023. [https://fortress.wa.gov/dnr/geologydata/publications/data_download/ger_portal_geophysics.zip]

Weaver, C. E., 1916, The Tertiary formations of western Washington: Washington Geological Survey Bulletin 13, 327 p., 6 plates. [https://www.dnr.wa.gov/Publications/ger_b13_teriary_form_western_wa_1.pdf; https://www.dnr.wa.gov/Publications/ger_b13_teriary_form_western_wa_2.pdf]

Wells, R. E.; Weaver, C. S.; Blakely, R. J., 1998, Fore-arc migration in Cascadia and its neotectonic significance: Geology, v. 28, no. 8, p. 759–762. [https://doi.org/10.1130/0091-7613(1998)026<0759:FAMICA>2.3.CO;2]

White, C. A., 1888, On the Puget group of Washington Territory: American Journal of Science, 3rd series, v. 36, no. 215, p. 443–450. [https://ajsonline.org/article/62693.pdf]

Wiedenbeck, Michael; Allé, P.; Corfu, Fernando; Griffin, W. L.; Meier, Martin; Oberli, Felix; Von Quadt, Albrecht; Roddick, J. C.; Spiegel, W., 1995, Three natural zircon standards for U-Th-Pb, Lu-Hf, trace element and REE analyses: Geostandards Newsletters, v. 19, p. 1–23. [https://doi.org/10.1111/j.1751-908X.1995.tb00147.x]

Williams, I. S., 1997, U-Th-Pb geochronology by ion microprobe. In McKibben, M. A.; Shanks III, W. C.; Ridley, W. I., editors, Applications of microanalytical techniques to understanding mineralizing processes: Reviews in Economic Geology, v. 7, p. 1–35. [https://doi.org/10.5382/Rev.07]

Willis, Bailey, 1898, Some coal fields of Puget Sound: U.S. Geological Survey Annual Report, 18th, Part 3, p. 393–436.

Wolfe, J. A., 1961, Age of the Keechelus andesitic series of the Cascade Range, Washington. *In* Short papers in the geologic and hydrologic sciences, articles 147-292: U.S. Geological Survey Professional Paper 424-C, article 232, p. 228–230. [https://doi.org/10.3133/pp424C]

Wolfe, J. A., 1968, Paleogene biostratigraphy of nonmarine rocks in King County, Washington: U.S. Geological Survey Professional Paper 571, 33 p., 7 plates. [https://doi.org/10.3133/pp571]

Appendix A. Geophysical Methods

GRAVITY

Overview and Purpose

Lateral changes in isostatic gravity result from density changes within rocks of the mid to upper crust. Gravity surveys are especially useful in delineating steeply dipping contacts between two rock bodies that have a large contrast in density. Areas of high gravity indicate that high-density rocks (for example many igneous and metamorphic rocks) are closer to the surface. Areas of low gravity indicate less-dense material, such as sedimentary basins that contain near-surface, low-density sediments. Gridding gravity measurements creates a map that outlines areas of high gravity and low gravity. Gravity data, paired with other measurable geophysical constraints, allow us to create models of the subsurface that quantitatively predict observable data. When combined with surficial geologic information and density measurements of surficial rocks, gravity data are powerful for modeling the subsurface. The goals of the gravity survey conducted for this mapping effort are to: (1) delineate density contrasts within the subsurface, (2) determine length and geometry of known structures, (3) identify previously unknown structures, and (4) provide geophysical constraints for forward modeling of the subsurface.

Description of Method

FIELD METHODS AND SAMPLED LOCATIONS

Data collected with a Scintrex CG-6 meter (Serial #19050174), supplement older datasets compiled by Finn and others (1991). We use the gravity base station ENUM (Washington Geological Survey, 2023b) to tie our data to the US gravity network. Gravity station spacing at roughly 2 km generates a coarse grid over a large area. In areas where known structures exist or initial gravity data collection showed a significant gradient, station spacing is 1 km to provide greater resolution. For modeled cross section lines, station spacing is roughly 250 m along the line, as access warrants. Selecting sites that avoid great topographic relief as much as possible reduces field terrain corrections. Sites with minimal tree cover maximize the effectiveness of the GPS unit (Javad Triumph-2). When tree cover is unavoidable, lengthening the recording time of the GPS unit accordingly provides the best possible vertical accuracy in elevation measurements.

DATA REDUCTION AND PROCESSING

A Javad Triumph-2 differential GPS unit provides the horizontal and vertical position of each station. The proprietary Javad Justin3 software allows for careful data editing and post-processing for differential correction using NOAA and the National Geodetic Survey's Continuously Operating Reference Stations within 70 km of the study area. After processing, typical positional accuracy is 0.15 m in the vertical and horizontal. Lidar elevation replaces GPS elevation in areas where lidar data are high-resolution and GPS elevation is suspect. We apply the factory gravimeter calibration constants to each gravity observation, augmented by correction factors obtained from the Mount Hamilton calibration loop east of San Jose, CA (Barnes and others, 1969), and Earth tide corrections, to produce observed gravity values. The data reference is the International Gravity Standardization Net of 1971 (Morelli, 1974) and the reference ellipsoid is the Geodetic Reference System of 1967 (International Association of Geodesy and Geophysics, 1971). The assumed linear drift between base-station ties results in a maximum gravity reading error of 0.05 mGal.

Gravity data reduction formulas for the free-air anomaly are standard (for example, Telford and others, 1990; Swick, 1942) and applying Bouguer, Earth curvature, and terrain corrections out to 166.7 km from each station produces a complete Bouguer anomaly. Terrain corrections are a combination of a field-based component (to a radius of 68 m using the Hayford system; Plouff, 2000) and a computer-generated component (using 30-m USGS DEM digital grids). To assist in the interpretation of mid- to upper-crustal density contrasts, the complete Bouguer anomaly is further reduced to an isostatic anomaly by applying formulas that adjust for long-wavelength variations, such as those caused by the existence of a crustal root and (or) upper-mantle density contrasts. An Airy-Heiskanen model (Heiskanen and Vening-Meinesz, 1958) produces the isostatic correction, assuming a 25-km-thick crust at sea level and a crust-mantle density contrast of 400 kg/m^3. All parts of the data reduction process assume a standard reduction density of 2,670 kg/m^3. Gravity readings and computed anomalies are in the Data Supplement.

Uncertainties in the gravity data are predominantly due to uncertainty in vertical position and the terrain corrections. Estimating elevation data uncertainties in this study is difficult due to a lack of ground-truthing available. We estimate uncertainties of around 0.15 m on average and a maximum of 1.5 m. This results in an average uncertainty from elevation of 0.03 mGal, up to a maximum of 0.30 mGal. The uncertainty associated with terrain corrections is generally only 5–10 percent of the actual correction. This results in an average terrain-correction uncertainty of 0.08–0.15 mGal but varies according to topography. Average uncertainty in steep and hilly regions is 0.12–0.23 mGal, whereas average uncertainty in flatter areas is 0.05–0.1 mGal. Based on these terrain uncertainties, gravity anomalies of 0.5–1 mGal and greater, supported by multiple observations, reflect interpretable density variations in the upper crust.

The minimum-curvature algorithms in the GIS software package Geosoft Oasis Montaj® transform our point isostatic anomaly data into gridded surfaces. The maximum horizontal gradient (referred to as 'max-spots'), calculated using the curvature analysis methodology of Phillips and others (2007), quantitatively locates strong and linear boundaries between rocks in the subsurface that have substantial density differences.

HAND SAMPLE DENSITIES

We collected bedrock samples throughout the study area for laboratory analysis. We weighed samples using an A & D company limited FX-3000i WP analytical balance. Three measurements per sample combine to determine density: a dry weight in air, a submerged (water-saturated) weight, and a water-saturated weight in air. While these measurements produce grain density, saturated bulk density, and dry bulk density, saturated bulk density best reflects subsurface conditions and was therefore referenced for modeling.

GEOMAGNETICS

Overview and Purpose

Magnetic surveys map the changes in the earth's magnetic field due to local magnetic sources at high resolution. This method delineates contacts between geologic units of contrasting magnetic properties, particularly in the mid to upper crust. A large number of magnetic profiles help to precisely determine magnetic contacts and trace them across a map area. Individual profiles, coupled with magnetic susceptibility measurements of surficial rocks, are powerful geophysical constraints for 2D subsurface modeling.

Aeromagnetics: Survey Specifications and Processing

Aeromagnetic data used in this study were acquired in 1997 (Blakely and others, 1999) via low-flying aircraft with a stinger-mounted magnetometer. North-south flight lines are 0.4 km apart, with east-west tie lines spaced at 8 km. These aeromagnetic measurements are interpolated to a projected, rectilinear grid using a bidirectional gridding algorithm within the GIS software package Geosoft Oasis Montaj. Another filter reduces this anomaly to the magnetic pole, more closely centering anomalies over their sources for map-view interpretation.

Hand-sample Properties: Description of Method

We collected bedrock samples throughout the study area for laboratory analysis. Magnetic susceptibility measurements taken with a KT10 Kappa Meter accompany rock sample density measurements, and we use the same meter to collect direct readings from outcrops where possible. Weathering tends to replace denser minerals with less dense weathering products and turn magnetite into less magnetic minerals like hematite. Our direct measurements also do not account for the component of remanent magnetization that adds to a rock's total magnetization. Therefore, all our measured rock densities and susceptibilities from surface outcrops (found in the Data Supplement) can be considered minimum values.

Survey Specifications And Processing

Volume susceptibility measures the magnetic susceptibility of a specific volume of rock regardless of sample size. Attempts to measure volume susceptibility on small cutting samples yield susceptibility measurements much lower than would be measured on an outcrop, a result of the instrument sampling a smaller volume of material than available in an outcrop. In this study, we convert volume susceptibility measurements of small samples to mass susceptibility following Ali and others (2015), as described below, then use a standard to convert the mass back to a corrected volume susceptibility. The advantage of measuring mass magnetic susceptibility is that it removes any effects due to anomalous porosity, which can affect the volume magnetic susceptibility measurements. This includes the intrinsic porosity of the individual drill cuttings and the porosity of the vial of very small samples caused by vacant space between cuttings. Drill cuttings of different sizes with an identical mineralogy will give exactly the same mass magnetic susceptibility value after this conversion.

QUANTITATIVE CROSS-SECTION MODELING

Overview and purpose

Quantitative 2D forward modeling of cross sections constrained by potential-field data provides insights into subsurface unit and fault geometry that go beyond qualitative interpretations of map-view data. This technique helps provide the best possible interpretation of fault type (for example normal, reverse, or strike-slip), fault dip in the upper crust (for example steep or shallow), and offset across the fault on units with particularly strong physical property contrasts with surrounding rocks. This method also can identify blind faults that have little surface expression and are difficult to capture via surface geology observations.

Description of Method

GM-SYS software (part of Geosoft Oasis Montaj®) provides the platform for computing the sum effect of blocks of rock in the subsurface in a 2D cross section on both the gravitational and geomagnetic fields of the Earth. This is a forward-modeling method. This means the operator hypothesizes which rock types are in the subsurface, their location, and their volume, and the GM-SYS program predicts the total fields that result from that particular model. The operator's responsibility is to refine the hypothesis until the predicted potential-fields match the data measured in the field. This ensures that any cross section interpretation of the subsurface matches two additional data types (for this study, gravity and magnetism) in addition to the surface geology, and thus reduces the number of potential hypotheses for the subsurface geometry of rocks.

Several lines of data constrain this process in addition to the gravity and aeromagnetic data. Surface geologic observations define rocks that are in the model's near-surface topography, and lab measurements of density and magnetic properties of hand samples from the surface inform rock properties. Also essential is the knowledge of the operator and collaborators in the project about the geologic history, expected stratigraphy in the subsurface, and structural geometries that are physically possible based on standard geologic mapping and cross section construction techniques.

Within these constraints, there is often a strong possibility that multiple subsurface geometries fit the gravity and magnetic data within error. Therefore, care in the construction of models helps define which parts of the subsurface model are well-constrained with the fewest alternative hypotheses and which parts could have multiple possible geometries. In general, potential-field data provide strong constraints on the position and dip of simple, steeply dipping boundaries that juxtapose rocks with strong differences in physical properties. Potential-field data provide a poor constraint on horizontal boundaries or boundaries between rocks with little contrast in physical properties. Depth of sub-horizontal stratigraphic boundaries within sedimentary rocks is particularly suspect and is never well-constrained without the addition of high-quality well logs or reflection-seismic data. Depth of sub-horizontal boundaries between units of strongly contrasting properties is resolvable but dependent on uncertainties in the physical properties of those units. In those cases, depth of a boundary can trade off with density or magnetism of the rocks.

Our modeling approach first constructs initial simplified models, including uniform packages of sediment, sedimentary rock, metamorphic rock, or volcanic rock to fit the overall long-wavelength features in the gravity and magnetic data. Our model space extends beyond the end of the models shown in this report to avoid edge effects due to truncated subsurface volumes. Adding detail in the stratigraphy and decreasing the size of blocks after the major fit allows modeling of smaller-scale features that fit shorter wavelength anomalies, particularly near the surface. During each iteration, we test possible options for physical properties of rocks and geometries of boundaries permitted by the surface geology observations and measured rock property constraints. Throughout the process of testing many variables, we conclude that we have a good fit if each model iteration produces a similar solution to fit the data.

Appendix B. Geochronology

RADIOCARBON DATING

Overview

Radiocarbon (^{14}C) dating is based on the radioactive decay of ^{14}C to ^{14}N. The half-life of ^{14}C is about 5,700 years. This makes the technique useful for dating organic material younger than about 45,000 years old, and especially younger than about 35,000 years old. We use ^{14}C dating on charcoal and other organic material within sedimentary units to help constrain their age of deposition.

Sample Collection and Preparation

We collected a charcoal sample from a glacial outwash deposit (age site GD3) and placed the sample in a zip-lock bag. As soon as practical, we air-dried the sample to prevent growth of plant or microbial organisms. We further examined and cleaned the sample as needed to exclude modern organic material (such as rootlets) that could have contaminated the analysis with post-depositional carbon. We placed the final sample in a fresh zip-lock plastic bag. We then mailed the sample to the DirectAMS lab for analysis.

Analytical Methods

The following text is reproduced with little modification from the DirectAMS website at www.directams.com/process and describes their general procedure:

Samples are photographed and inspected for appropriateness of the requested services. Any discrepancies are discussed with the submitter. Samples then proceed through portioning/subsampling, physical and chemical pre-treatment protocols, production of CO_2 by combustion or acid digestion, reduction of CO_2 to graphite, preparation of graphite for measurement, measurement of carbon isotopes by Accelerator Mass Spectrometer (AMS), and data analysis, as appropriate for the type of sample. DirectAMS operates two different AMS instruments, an NEC Pelletron 500 kV and an IonPlus MICADAS 250 kV. Design differences between these instruments are detailed on the DirectAMS website; the general principle in the analysis is the same.

DirectAMS reports results in units of percent modern carbon (pMC) and the uncalibrated radiocarbon age before present (BP). All results have been corrected for isotopic fractionation with an unreported $\delta^{13}C$ value, measured on the prepared carbon by the AMS. The pMC reported requires no further correction for fractionation. After ~40,000 years, less than 1% of the original ^{14}C remains in a sample, reducing the precision of measurement. For DirectAMS, any measurement that falls below 0.369 pMC, exceeding 45,000 years old, is not distinguished from the measured level of background carbon.

Results

We collected and analyzed one charcoal sample from glacial outwash (unit Qgo) exposed in a borrow pit in the southeast corner of the quadrangle (age site GD3). The age appears too old to distinguish with the radiocarbon technique, and the sample likely is detrital and does not accurately date the deposit. Summary age data are in Table 1, with more details in Table B1 below; laboratory reports are in the Data Supplement.

Table B1. Radiocarbon geochronology sample information and results.

Sample ID	GD3	An isolated piece of charcoal approximately 8 cm x 4 cm x 6 cm was collected from an exposure in a borrow pit approximately 2 m below the glacial outwash deposit surface. Upon cleaning and preparing it for lab analysis we noticed the sample was partially cemented with silica that made us wonder about the possibility that the sample had been re-mobilized from nearby older Tertiary sedimentary or volcaniclastic deposits. We expected the outwash deposit to be less than 30 ka and the measured ^{14}C age supports the possibility that the carbon may be much older than the glacial outwash deposit.
Lab ID	D-AMS 052675	
TRS location	Sec. 26, T21N R8E	
Latitude (degrees)	47.2749	
Longitude (degrees)	-121.7543	
Elevation (ft)	1,444	
Material	Charcoal	
Geologic unit	Qgo	
Age (^{14}C yr BP)	42,018	

U-PB ZIRCON DATING

Overview

U-Pb dating uses radioactive decay of uranium to estimate the crystallization age of uranium-bearing minerals. We sample rocks or sediment to assess the crystallization ages of zircons within the deposit, and thereby estimate the igneous rock crystallization age or constrain the maximum possible age of sediment deposition: meaning that the sediment deposit must be younger than the zircons within it. We analyzed 110 zircons from one sample of sedimentary rock; volcanic deposits may be analyzed with fewer zircons (n=39 for age site GD2) because most or all zircons are expected to be of similar age. Each zircon yields a separate age. Zircons from a sediment sample often originate from rocks of different age, and thus zircon age spectra contain information about sedimentary provenance.

Sample Collection and Preparation

We generally collect about 2–10 kg of freshly exposed rock per sample, while avoiding contact with soil or other surface deposits that could introduce extraneous zircons; weathering and alteration do not usually affect the age of zircon and therefore pose no concern for this technique. We send our samples to ZirChron, LLC, for mineral separation using the following procedure:

Samples are pressure washed with water and then disaggregated using an Electro Pulse Disaggregator (EPD, Marx generator) at 1 Hz with discharges of ~250 kV for 15 minutes. Any clasts >500 µm are crushed in a crusher or pulverizer. Using stainless steel sieves, the fraction between 350 µm and 25 µm is retained and then processed using a Wilfley water table, Frantz paramagnetic separator, and a two-step (3.00 g/cm^3 and 3.32 g/cm^3) heavy liquid methylene iodide separation. Zircon grains from each sample are hand selected and mounted in epoxy, polished to expose the grain centers, and regions suitable for analysis are identified from optical imaging.

Analytical Methods

The following text is reproduced from a technical write-up by the Washington State University Radiogenic Isotope and Geochronology Laboratory with minimal modification:

Zircon U-Pb ages are measured at the Radiogenic Isotope and Geochronology Lab (RIGL) at Washington State University using an Analyte G2 193 excimer laser ablation system coupled with a Thermo-Finnigan Element 2 single-collector inductively coupled plasma mass spectrometer. The laser parameters are 25-µm-diameter spot size, 10 Hz repetition rate, and fluence of ~5.0 J/cm^2. For the U-Pb measurement, we mostly followed the method of Chang and others (2006) and Gaschnig and others (2010), except for the use of a 193-nm laser system. A 10-second blank measurement of the He and Ar carrier gasses (laser off) before each analysis is followed by 250 scans across masses ^{202}Hg, ^{204}Pb+Hg, ^{206}Pb, ^{207}Pb, ^{208}Pb, ^{232}Th, ^{235}U, and ^{238}U during ~30-second laser ablation periods. Analyses of zircon unknowns, standards, and quality control zircon grains are interspersed with analyses of external calibration standards, typically with 10–12 unknowns bracketed by multiple analyses of two different zircon standards (Plešovice and FC-1). The Plešovice standard (337 Ma; Sláma and others, 2008) is used to calibrate the ^{206}Pb/^{238}U and ^{207}Pb/^{23}5U ages, and the FC-1 standard (1,099 Ma; Paces and Miller, 1993) is used for calibration of ^{207}Pb/^{206}Pb ages owing to its high count rate for ^{207}Pb (~2–4 times higher than that of Plešovice). Zircon 91500 (1,065 Ma; Wiedenbeck and others, 1995), Fish Canyon Tuff (~27.5 Ma; Lanphere and Baadsgaard, 2001), and Temora2 (417 Ma; Black and others, 2004) are used as quality control standards. Data are processed offline using the Iolite software (Paton and others, 2011). Common Pb correction is performed using the ^{207}Pb method (Williams, 1997).

Results

We collected and analyzed two samples (age sites GD1 and GD2). GD1 is from unit ΦEvaₒ—a sandstone interbed from just above the contact with the Puget Group. The lab provided ages from the youngest statistical population age spectra (see Data Supplement for full data). GD2 is from unit Ꚗigbd—a gabbroic diorite that intruded volcaniclastic deposits of unit ΦEvc. Crystallization ages from a coherent group of ages using the TuffZirc algorithm (Ludwig, 2003) were computed by the lab for GD2. Age interpretations are summarized in Table 1 and B2.

Table B2. U-Pb geochronology sample information and results.

Map ID	GD1	Sandstone within unit ΦEva$_o$ Field description: Light orange tan medium–coarse sandstone with less than 1-cm-thick layers of pebbles. Sample taken from a planar, 5–10-cm-thick bed. East dipping, with no obvious fossils or bedding features. Estimated outcrop thickness of 6–9 m. Relatively resistant ridge of sandstone among volcanics and volcaniclastics.
Field sample ID	EGT143	
TRS location	Sec. 13, T21N R7E	
Latitude (degrees)	47.2998	
Longitude (degrees)	-121.8624	
Elevation (ft)	1,717	
Number of grains analyzed	56	
Colocated analyses	G7 and TS13	
Geologic unit	ΦEva$_o$	
Age (Ma) ±2σ	35.8 ±0.4	
Age type	Depositional age	

Map ID	GD2	Gabbroic diorite Field description: Intrusive, fine grained, intermediate composition: weathers to white and green tan; dark gray where fresh. Interlocking crystals of plagioclase, quartz, and hornblende, and possible minor pyroxene(?). Epidote present, <1%. Plutonic. Weathered surfaces are more white and green, can see acicular hornblende.
Field sample ID	EGT067	
TRS location	Sec. 22, T21N R8E	
Latitude (degrees)	47.2872	
Longitude (degrees)	-121.7803	
Elevation (ft)	2,309	
Number of grains analyzed	31	
Colocated analyses	G9 and TS17	
Geologic unit	Migbd	
Age (Ma) ±2σ	18.9 ±0.2	
Age type	Crystallization age	

Appendix C. Geochemistry

Overview

We use major- and trace-element analyses to classify igneous rocks in the map area and to aid in their identification and correlation. Our 12 samples span a range of rock types and range from Eocene to Miocene.

Sample Collection and Preparation

We select samples for geochemical analysis from intrusive, volcanic, and volcaniclastic rocks. We use hammers, usually a small sledgehammer, to break off the freshest pieces. Where we are concerned about possible contamination from hammer streaks, we try to remove those, usually by using fragments of the same sample to scrape or break off any streaks. We generally submit between ~100 and ~200 g of the freshest available material for lab analysis, except where sample sizes are necessarily smaller.

Analytical Methods

We reproduce the following abbreviated methods directly from documents provided by the ALS Geochemistry Laboratory in Vancouver, British Columbia; only general descriptions of methods are provided by ALS on their website:

Major element percentages are determined on a fused bead after acid digestion using inductively coupled plasma-atomic emission spectroscopy (ICP-AES) (ALS analysis code ME_ICP06). A prepared sample (0.1 g) is added to lithium metaborate/lithium tetraborate flux, mixed well, and fused in a furnace at 1,025 °C. The resulting melt is then cooled and dissolved in an acid mixture containing nitric, hydrochloric, and hydrofluoric acids. This solution is then analyzed by ICP-AES. Results are corrected for spectral inter-element interferences.

Loss on ignition (LOI) (ALS analysis code OA_GRA05) is determined using a 1 g sample, placed in an oven at 1,000 °C for one hour, cooled, and then weighed again. The percent loss on ignition is calculated from the difference in weight before and after ignition.

Trace element concentrations are determined using inductively coupled plasma-mass spectroscopy (ICP-MS) (ALS analysis code ME_MS81). Samples are prepared following the same lithium borate fusion and digestion procedure as applied in ICP-AES analyses, but are subjected to an additional lithium borate fusion and an acid digestion procedure prior to analysis on the ICP-MS.

Results

We obtained results for 12 samples. Sample locations are shown on the Map Sheet; analytical data are in the Data Supplement.